

5-2023

# Mitral Valve Imaging and Biomechanics: A Workflow Towards Computational Modeling and Validation

Sam Stephens  
*University of Arkansas-Fayetteville*

Follow this and additional works at: <https://scholarworks.uark.edu/etd>



Part of the [Animal Experimentation and Research Commons](#), [Biomechanics and Biotransport Commons](#), and the [Biomedical Devices and Instrumentation Commons](#)

---

## Citation

Stephens, S. (2023). Mitral Valve Imaging and Biomechanics: A Workflow Towards Computational Modeling and Validation. *Graduate Theses and Dissertations* Retrieved from <https://scholarworks.uark.edu/etd/5095>

This Thesis is brought to you for free and open access by ScholarWorks@UARK. It has been accepted for inclusion in Graduate Theses and Dissertations by an authorized administrator of ScholarWorks@UARK. For more information, please contact [scholar@uark.edu](mailto:scholar@uark.edu).

Mitral Valve Imaging and Biomechanics:  
A Workflow Towards Computational Modeling and Validation

A thesis submitted in partial fulfillment  
of the requirements for the degree of  
Master of Science in Biomedical Engineering

by

Sam Stephens  
Missouri University of Science and Technology  
Bachelor of Science in Physics, 2013  
University of Arkansas  
Bachelor of Science in Mechanical Engineering, 2016

May 2023  
University of Arkansas

This thesis is approved for recommendation to the Graduate Council.

---

Morten O. Jensen, Ph.D.  
Thesis Director

---

Hanna Jensen, Ph.D.  
Committee Member

---

Paul Millett, Ph.D.  
Committee Member

## **Abstract**

The mitral valve serves a critical role in healthy cardiac function by ensuring the unidirectional flow of oxygenated blood from the left atrium into the left ventricle. It experiences the highest pressures found within the heart and its closure is the result of a complex interaction of several different structures that, furthermore, are unique to each individual. Despite the valve's vital role however, the specific function of these constituent structures is not fully understood. This, confounded by its asymmetric, personalized nature, make surgical interventions for the mitral valve far less effective than for its neighboring aortic valve. Efforts to overcome this have been made through the lens of computational simulation, in which the valve is studied virtually and procedures may be planned. The quality and reliability of these simulation results are only as good as the inputs that the simulation model receives.

This study proposes and evaluates a workflow by which high-quality biomechanical inputs are obtained for computational input and validation. To account for individual variation, all steps are performed on the same valve such that a direct correspondence is made between geometry, stress/load distribution and the resulting coaptation. Ultrasound *in vivo* measurements are made so that custom tailored mounting hardware can be manufactured. This hardware is used to support the valve in a physiologically appropriate manner for  $\mu$ CT imaging in both the open and closed configurations. Scanning within a fluid medium, to prevent tissue desiccation and other detrimental effects, is made possible through a DiceCT tissue staining procedure. High resolution, 3D imagery is obtained for the open valve whereas only a relatively quick set of projection images is obtained for the closed configuration. Registration between open and closed imagery is accomplished by localizing aluminum oxide fiducial markers that are bound to the leaflet surface. Subsequent image analysis is performed to isolate the tissue and place the data in

the proper format for computational use. The valve is then closed under known pressure while chordal forces/strains are simultaneously recorded to provide loading conditions.

The effectiveness of the workflow is illustrated through two animal experiments. Incomplete results were obtained from the first experiment as the tissue degraded significantly during a prolonged period of  $\mu$ CT downtime. The second experiment resulted in good quality ultrasound imagery, leading to the creation of customized mounting hardware, yet the remainder of the process was still in progress at the final stages of this document. Computational modeling is still ongoing, yet some preliminary results are presented which show the geometry from the first animal experiment tending towards closure.

## **Acknowledgements**

I would first like to express my sincere gratitude to Dr.'s Morten and Hanna Jensen for their continual support. From when I first began working with mitral valves in my senior design project, their passion for research was contagious. I would also like to thank my final committee member; Dr. Paul Millett. His computational methods class was my favorite from my undergraduate work and I have been grateful for the opportunity to continue to work with him. I must of course also thank collaborators Dr.'s Neil Ingels and Jonathan Wenk for their insightful advice and valuable assistance.

Next, I would like to thank the students who I have worked with, both graduate and undergraduate. My fellow CB lab graduate students; Mads Ancker, Kaitlyn Elmer, Maxwell Bean and Megan Laughlin have made the journey much more enjoyable. Undergrads with whom I have worked are too numerous to name in full, but include Marinna Tadros, Hudson Surber, Kaylee Henry and Joseph Berryman.

MicroCT scans conducted for this research were performed at the University of Arkansas MicroCT Imaging Consortium for Research and Outreach (MICRO), which was originally funded as part of a National Science Foundation Major Research Instrumentation grant (BCS-1725925). I would like to specifically thank and acknowledge Manon Wilson for her invaluable assistance and advice with scanning. Without her, quite simply, the imaging work would not have been possible.

I would finally like to thank my family. Laura, your help, support, and love are more valuable than you know. It's to my Dad that I owe my appreciation for all things mechanical. And without my Mom's unwavering belief and support, none of this would have happened.

## Table of Contents

I. Introduction .....	1
II. Methods .....	5
2.1 <i>In vivo</i> Measurements.....	5
2.1.1 Ultrasound .....	7
2.1.2 Electrocardiogram Acquisition.....	9
2.1.3 Cardiac Pressure .....	10
2.2 Hardware Manufacture.....	11
2.2.1 Symmetric Hardware .....	11
2.2.2 Point-Driven Hardware.....	12
2.3 Imaging.....	13
2.3.1 Imaging System .....	13
2.3.2 DiceCT Staining .....	17
2.3.3 Fiducial Markers.....	19
2.3.4 Closed-Valve Imaging.....	21
2.4 Data Analysis .....	22
2.4.1 Hardware Subtraction.....	24
2.4.2 Fiducial Localization .....	28
2.5 Biomechanics .....	33
2.5.1 Vacuum Valve Closure.....	33

2.5.2 Chordal Force Gauges .....	34
2.5.3 Papillary Muscle Force.....	38
2.6 Finite Element Simulations.....	40
2.6.1 Geometry Simplification .....	41
2.6.2 COMSOL Modeling.....	42
III. Pilot Data .....	42
IV. Conclusion .....	46
V. Future Work .....	46
References.....	48
Appendix A – List of Relevant Publications (Chronological).....	53
Appendix B – Fiducial Localization Mathematics .....	54
Appendix C – IACUC Protocol .....	63

## I. Introduction

The mitral valve, one of four valves in the heart, separates the left atrium and left ventricle. It acts as a one-way valve, permitting blood flow from the atrium to ventricle but preventing flow in the opposing direction. During systole, when the left ventricle contracts to send blood through the aorta to the body, the valve closes, ensuring maximum cardiac output of oxygenated blood. In diastole, the mitral valve opens to permit ventricular filling from the atrium. The mitral valve, like the other heart valves, opens and closes in response to a trans-valvular pressure differences; closing when the inferior/ventricular pressure exceeds that of the superior/atrial. The pressures to which the mitral valve is subject are the highest found within the heart, producing forces on the order of 10 N each time the heart beats [1]. This force is supported by two leaflets, generally between 3 and 5 mm at thickest and tapering to be much thinner at the free edges [2]. These thin leaflets are further supported by a complex network of chordae tendineae which anchor into the ventricular wall through two papillary muscles. The chordae, long thought to anchor the leaflets and prevent prolapse, are now believed by some to guide the leaflets into their proper geometry prior to closure, whereupon the leaflets are largely capable of supporting the load. These structures are illustrated in Figure 1.

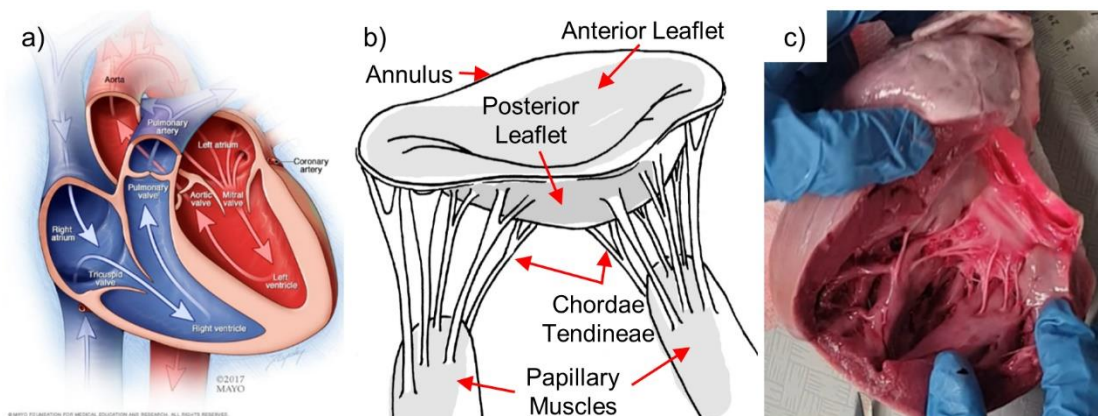




**Figure 1** – Heart and mitral valve anatomy; a) cut-away view of the heart showing blood flow, b) mitral valve structures and c) photo of actual, partially dissected mitral valve [3,4]

Given its crucial role within normal cardiac function, any mitral valve disorder can seriously affect the heart's performance. The most prevalent issues affecting the mitral valve are mitral prolapse and regurgitation. Mitral regurgitation is the leakage of blood, from the ventricle to the atrium, during valve closure. This results in incomplete ejection of oxygenated blood, depriving the brain and rest of the body. Some degree of regurgitation is normal and relatively harmless, presenting asymptotically, though elevated levels can become problematic, causing symptoms such as shortness of breath and cardiac arrhythmia [5]. Significant mitral regurgitation affects 1.7% of the US population, increasing to nearly 10% beyond the age of 75 [6]. Regurgitation may be degenerative, being caused by a structural issue with the valve itself, or ischemic, which is caused by alterations to normal valvular function, such as through ventricular remodeling. Mitral prolapse is characterized by floppy leaflets that bulge upwards into the atrium, often resulting in poor valve closure. Prolapse affects 2-3% of the population, and is generally an acquired disease rather than congenital, resulting from the degradation of connective tissues [7,8]. Many cardiac conditions occur concomitantly, and mitral prolapse frequently caused regurgitation. Severe cases of these disorders generally require surgical intervention to correct.

Catheter-based aortic valve replacement, since its development in the 1990's and first clinical use in 2002, has become a routine procedure with excellent survivability, upwards of 60% at three years [9-11]. A typical replacement, referred to as Transcatheter Aortic Valve Replacement (TAVR), takes a mere 3 hours (often as little as 1 hour) and requires only 2-3 days post-operative observation [12]. Typically comprised of a self or balloon-expanding Nitinol frame surrounding a tri-leaflet valve, generally of bovine or porcine pericardium tissue, these replacement valves

are delivered by catheter through a femoral insertion [13]. The first attempts at mitral replacement utilized these well-established TAVR valves, placed in the mitral position. Outcomes from initial studies were generally poor, with high morbidity and significant perivalvular leakage [14]. Unlike the generally round aortic valve, the mitral valve has a pronounced d-shape, leading to poor sealing between the native annulus and the exterior of the replacement valve. Anchoring is challenge as well, partially due to the complex subvalvular apparatus, but also due to a general lack of calcified tissue which is common to aortic valves. Replacement mitral valves must also not extend so far into the left ventricle as to obstruct the left ventricular outflow tract, further limiting anchoring options. Recent developments have improved mitral replacement, and clinical trials are ongoing, but much work likely remains before mitral replacement reaches the same level of reliability of the TAVR.

It is principally due to the issues with mitral replacement that the clinical focus is placed much more on valvular repair [15]. Common repairs involve the placement of an annuloplasty ring - rigid or flexible rings that force the mitral annulus to adopt a different contour, leaflet patches to close holes or suturing/trimming leaflets. While effective, these techniques are quite invasive, requiring open-heart surgery. As a result, minimally-invasive, catheter-based solutions are becoming increasingly prevalent. One such recently FDA-approved device is the MitraClip, which acts somewhat like a staple, extending by catheter through the mitral annulus and mechanically fastening the anterior and posterior leaflet margins. This prevents them from fully separating during diastole, altering the leaflet coaptation and ideally reducing/eliminating mitral regurgitation [16]. The Neochord is another example of a minimally-invasive device. Delivered through the intercostal space between the ribs, the Neochord acts as an additional or replacement chord, helping minimize leaflet prolapse [17].

While these repair techniques generally result in superior outcomes to replacement, challenges remain. The mitral valve is inherently a complex structure and outcomes are difficult to predict. Furthermore, mitral valve function is often linked to other compounding effects, such as left ventricular remodeling. Computational methods have the potential to investigate the mechanisms of mitral function *in silico*, permitting more thorough investigation than is possible *in vivo*. Several mitral models have previously been reported upon with varying degrees of complexity [18-20]. No matter how detailed the model however, the results will not be reliable without quality inputs for valvular geometry, load distribution and tissue mechanics. The tissue mechanics in particular has been challenging to detail accurately as the mitral valve is composed of several geometrically-complex, distinct tissues that are non-linear and inhomogeneous [21]. Benchtop measurements have certainly been conducted to investigate these properties, including uniaxial chordal stress-strain and biaxial leaflet analysis, collagen orientation, etc. [22-24]. Due to restrictions on minimum sample size however, these measurements naturally reflect something of a bulk parameter, missing the fine detail of the intricate valve.

This study aims to investigate these highly relevant material properties by computational iteration from some known, initial (open) geometry and loading, using an assumed property distribution. Comparison of the simulated deformation under these conditions with the known, closed-valve geometry permits adjustment of the material properties. By this process the properties are iterated until convergence between simulated and observed geometry is achieved. Major steps within the workflow, as well as the division of tasks between collaborators, are illustrated in Figure 2.

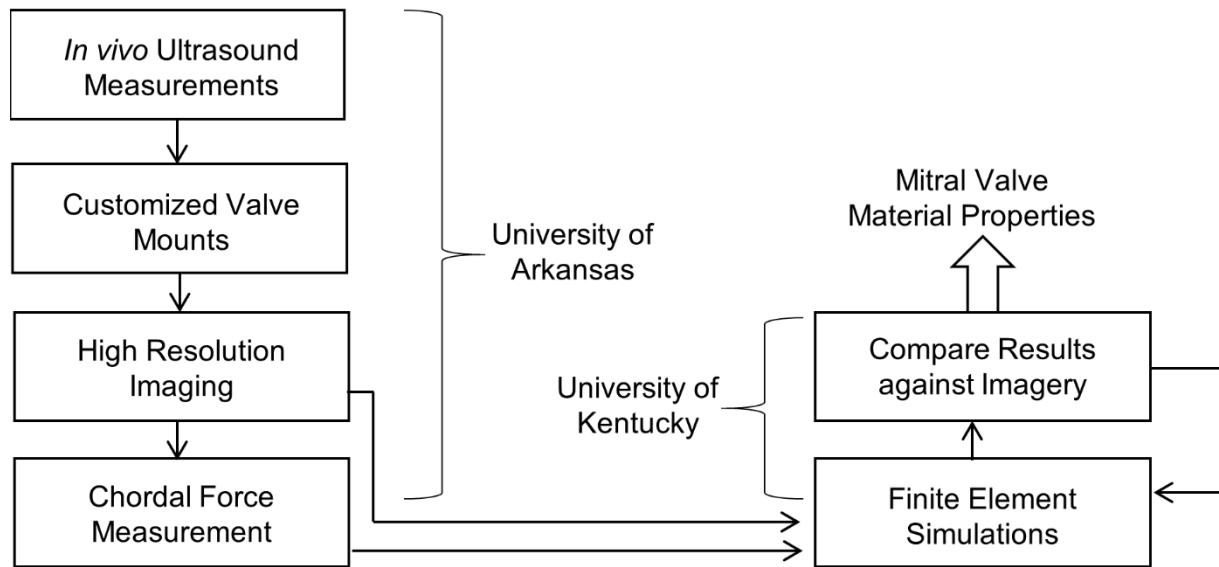


**Figure 2** – Summary of workflow to obtain computational estimates of mitral material properties.

## II. Methods

### 2.1 *In vivo* Measurements

Given the complex, 3D geometry of the native mitral valve, which is additionally a function of time within the cardiac cycle, any attempt to accurately model valvular dynamics must utilize *in vivo* imagery of the beating heart to capture the geometry. Fine structures, such as the CT, are generally not visible in *in vivo* imaging modalities, such as ultrasound, requiring subsequent *in vitro* imagery. To remain physiologically relevant however, this *in vitro* imagery must be conducted with the valve in a physiologically-mimicking state, accomplished through specialized mounting hardware. The creation of this hardware (section 2.2) utilizes *in vivo* geometry to inform its design through the annular profile and PM locations, both of which are specific to each valve and play a vital role in proper valve coaptation and overall function [25,26].

Many previous studies utilize flat annulus clamps, rather than the more physiological saddle-shape [27-29]. In part, this is due to the annulus' saddle-shape being poorly understood until

relatively recently. Other studies may elect to settle for a flat annulus as the construction of a contoured mount may be outside their study's scope. Nevertheless, it has been shown that a saddle-shaped annulus reduces leaflet stress and improves coaptation [25].

Additionally, benchtop force measurements rely on accurate loading of the valve. The valve closes principally due to the trans-mitral pressure developed across the valve during systole. This pressure naturally varies from individual-to-individual according to cardiovascular health.

A series of animal experiments were conducted to obtain the required geometry and pressure data. Pigs were used throughout the development of this workflow due to their anatomical similarity to humans, as well as the general availability of fresh/frozen pig hearts from local abattoirs. For the animal experiments, approximately 80 (176 pound) kg pigs were used. The animals were sedated by intramuscular injection and isoflurane was utilized as an inhaled anesthetic, along with continuous intravenous infusion of fentanyl in combination with ketamine. The pigs were prepared as per routine operating room procedures, including artificial ventilation and blood pressure monitoring, all while monitored by trained surgical staff. While sedated, valvular geometry and cardiac pressure was measured. The complete *in vivo* measurement system is illustrated in Figure 3.

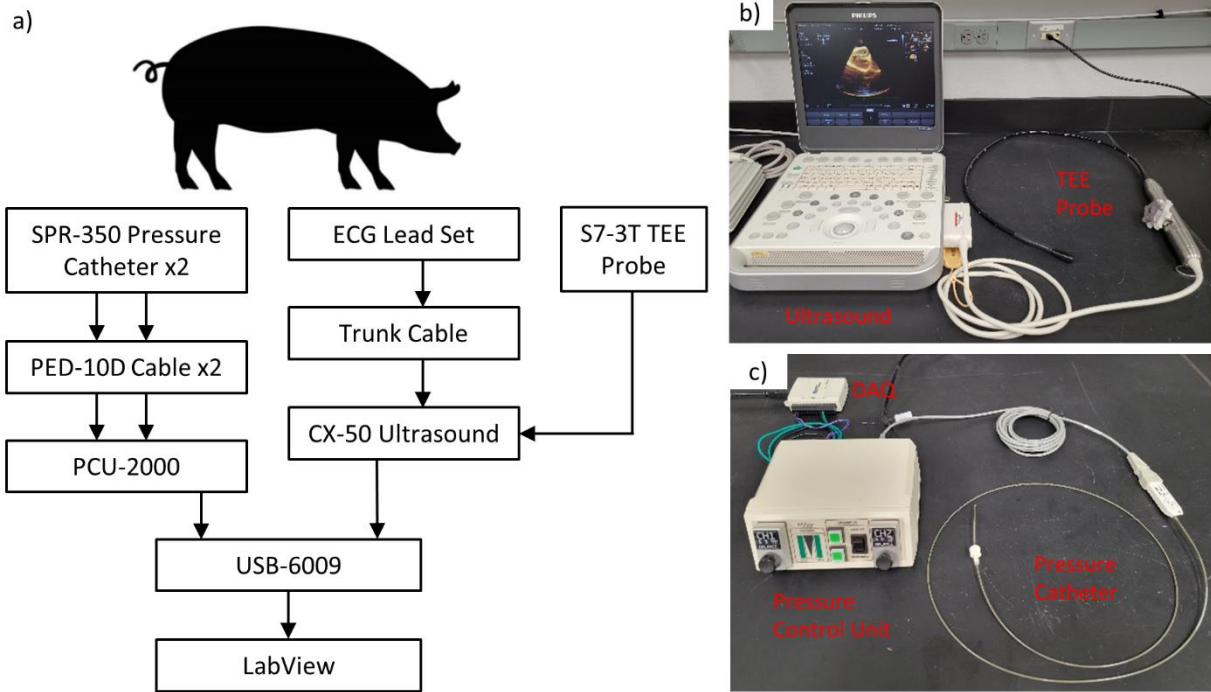


**Figure 3** – a) *In vivo* measurement system shown schematically, b) CX50 ultrasound with TEE probe and c) Millar pressure catheters and conditioning equipment

### 2.1.1 Ultrasound

Initial attempts to measure pertinent dimensions via epicardial, b-mode ultrasound were made at the conclusion of several unrelated animal trials but difficulty was experienced in obtaining consistent images that were directly aligned with our intended imaging plane. This was in large part due to the substantial movement of the heart relative to the ultrasound probe. It was concluded that image plane mismatch was ultimately likely, even with additional practice, and that a 3D ultrasound would likely be the best solution. To this end, a Philips CX50 portable ultrasound machine was purchased along with an S7-3T transesophageal echocardiography (TEE) probe. The CX50 is capable of time-resolved 3D imaging and can accept an ECG input for synchronization. Additionally, by using TEE the animal's chest no longer needs to be

opened, thereby reducing the overall stress experienced by the animal and quite possibly allowing the acquisition of images closer to the native, resting state.

The CX50 was purchased with Philip's QLab suite installed; a set of apps that permit on-board analysis and quantification of imagery. Of particular interest to this project is the Mitral Valve Navigator (MVN) app, which guide the user through selecting reference points such as commissure points, muscle locations, leaflet shape, etc. The software then performs a 3D fit to generate a model of the annulus and leaflets. Many clinically relevant parameters, such as (but not limited to) orifice area, leaflet prolapse volume and annular ellipticity are computed and displayed. While the outputs from MVN are intuitive and very clinically relevant, they do not provide excessive detail for hardware-generation purposes. Such as they are, reported dimensions are sufficient for hardware design as outlined in **Stephens, Plos**, (section 2.2.1), but not for more recently developed methods which utilize additional, arbitrary points (section 2.2.2) [4].

It has been shown that for some models of Philips ultrasound machines (but not the CX50), it is possible to directly export the 3D DICOM [30]. Despite extensive communication with Philips support however, it was not possible to perform such an export with the CX50, which would have allowed the identification of annular and PM geometry directly on a 3D model. Instead, the captured 3D (plus time) dataset was opened using the MVN app and all on-screen instructions were followed to orient the MV. In short, the end-diastolic frame was identified by the overlaid ECG trace and the sagittal, coronal and transverse planes aligned to the valve by the identification of anatomical landmarks. Once fully registered and oriented, the valve geometry was transferred to SolidWorks, where annular and PM geometry were extracted (section 2.2.2).

### ***2.1.2 Electrocardiogram Acquisition***

As valve-specific hardware is to be generated for specific time-points within the cardiac cycle (namely end-diastole and end-systole), the ultrasound imagery needs to be synchronized to the cycle. This is commonly achieved by simultaneous recording of inter-cardiac pressure or electrocardiogram (ECG). Given that cardiac pressures are already measured (section 2.1.3), it was initially planned to use this for synchronization, defining systole/diastole based upon the derivative of the pressure signal. While the CX-50 does indeed have an analog auxiliary input channel, the electric specifications were not conducive to direct import of pressure signals. While solutions were considered, such as a voltage divider to reduce the pressure output voltage to that of the CX-50's input level, it was determined to instead utilize ECG.

A trunk cable was used to connect the CX-50's low-level ECG input to a 3-contact lead-set. The CX-50 was software-configured to output the original ECG signal on its analog output channel. This ECG signal was displayed on-screen during ultrasound capture and was simultaneously obtained by the same data acquisition system used to acquire cardiac pressure measurements (section 2.1.2). Therefore, pressure and ECG are synced, and ultrasound and ECG are synced, so it is possible to synchronize pressure and ultrasound.

A 3-lead setup was used, with leads placed in the typical locations. The leads were placed in the typical locations as indicated on each individual lead - RA for right arm, LA for left arm and LL for left leg. When used on animals, the application site was first shaved to ensure good electrical contact. Due to electrical interference, bed warmers were not used underneath the animals as this greatly affected the ECG signal. The ECG setup and CX50 ultrasound are shown in Figure 3a and b respectively.



### ***2.1.3 Cardiac Pressure***

Cardiac pressure measurements were made by pressure sensing catheters. A Millar SPR-350S (5F diameter) Mikro-Tip pressure catheter (Millar, Inc., Houston, TX) was connected to a PCU-2000 pressure control unit via a PED-10D cable. Analog voltage signals were collected from the PCU-2000 by a National Instruments USB-6009 (National Instruments, Austin, TX) interfaced with LabVIEW (National Instruments) via USB to record the waveforms. The pressure waveform was sampled at a frequency of 1000 Hz. The ECG signal from the CX-50 ultrasound (section 2.1.2) was also collected simultaneously by the USB-6009. The pressure data acquisition setup is illustrated in Figure 3c. Acquisition of ultrasound and pressure/ECG data were both started manually as closely as possible to ensure ease of subsequent synchronization. The pressure catheters were placed within the ventricle to measure trans-mitral pressure. Atrial pressure was assumed to be 10 mmHg. This catheter was introduced apically and sealed with a purse-string suture, tied with 4-0 silk suture. The apical approach was selected over trans-aortic to not inadvertently damage the aortic valve or coronaries, particularly since the placement was not fluoroscope guided.

The annular geometry and PM locations needed for hardware customization (section 2.2) are taken at mid-systole and mid-diastole. Identification of these time points is done by examination of the ventricular pressure waveform. Mid-systole was defined as the midpoint between the pressure derivative's maximum and minimum whereas mid-diastole was taken to be the time point between the pressure derivative's minimum and maximum [1]. The identification of these time points permits corresponding times along the ECG waveform to be selected. As ECG is recorded synchronously (but separately) with both the ultrasound as well as pressure, the mid-systolic and mid-diastolic frames from the TEE dataset may be identified.

## 2.2 Hardware Manufacture

### 2.2.1 Symmetric Hardware

The creation of custom valve mounting hardware was previously detailed in **Stephens, Plos One** [31]. In summary, a set of predetermined valvular measurements are made *in vivo*, with these measurements being used to drive a parametric CAD (computer aided design) model (Figure 4). Such measurements include the septal-to-lateral diameter, commissure-to-commissure width, annular height and the distances from each papillary muscle tip to the mid-anterior annulus. With these measurements entered into the CAD models for the annulus clamp and muscle holders, they are 3D printed and post-processed to remove all support material.

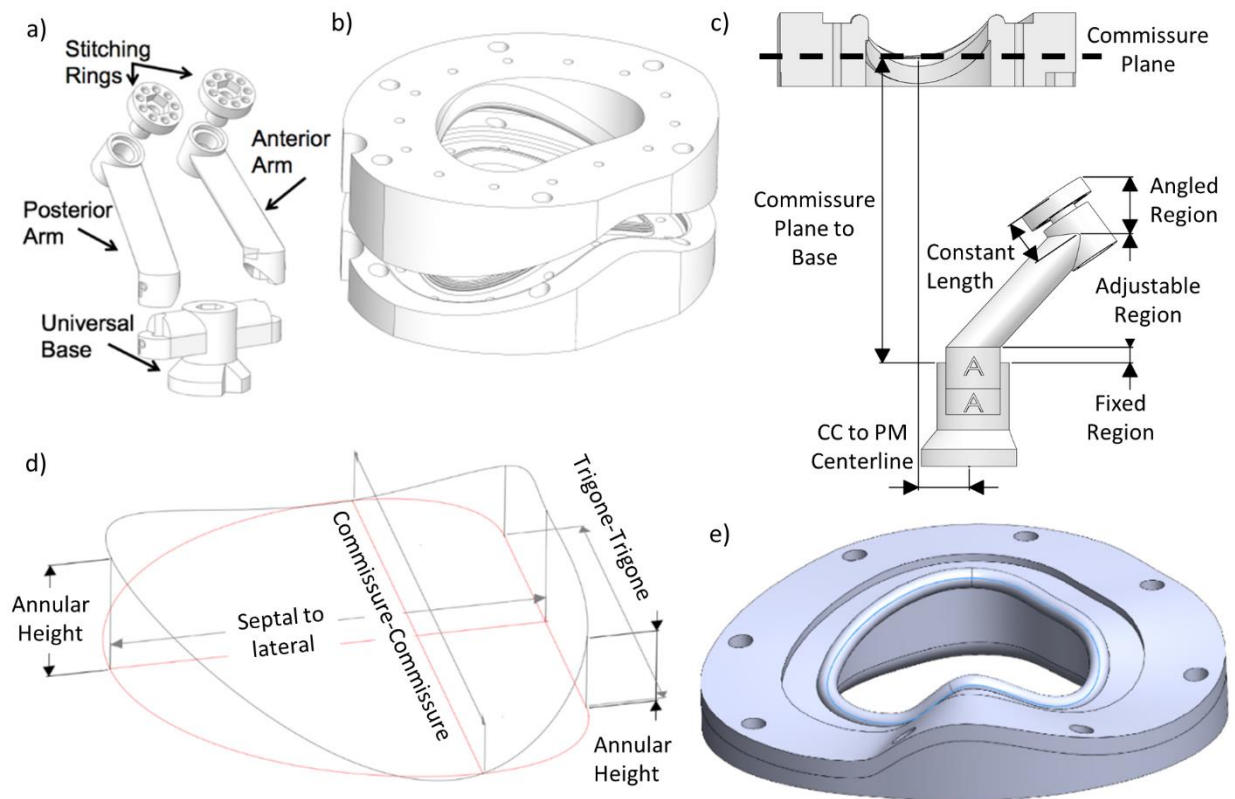


**Figure 4** – Valve mounting hardware, as previously described (left) and current (right); a) Papillary muscle holder, b) annulus clamp, c) dimensions for fitting papillary muscle holder relative to annulus clamp d) dimensions for fitting annulus clamp to valve, and e) new, spline driven clamp (input spline shown in blue)

### ***2.2.2 Point-Driven Hardware***

Recent work has updated the methodology somewhat from this above publication. It is now possible, given an obtain an arbitrarily set of (3D) coordinate points along the annulus, to use these to drive a spline fit to the annulus, an example of which is shown in Figure 4c. This creates a much truer representation of the mitral annulus as it captures the asymmetric nature of the complex valve structure. The clamp model has also been adapted from a solid modeling approach to surface modeling, which has proven to be much more robust when updating to new geometries. Other alterations since publication include the addition of identification numbers and conical fiducial markers to assist with later analysis (detailed further in section 2.4.1).

In order to generate such a set of annular points, the 3D ultrasound geometry was first oriented within QLab's MVN (section 2.1.1). Then, screen captures were taken while viewing the valve from each of the eight rotations about the z-axis. These captures were then imported into SolidWorks as sketch images, with each placed on a separate plane, separated by the corresponding angle within MVN. Once registered with one another, a 3D sketch was created and coordinate points manually placed along the annulus in each image plane. These points were then connected with a cubic spline, which formed the basis for the annular profile in the custom annular clamp.

Initial efforts were made to print hardware with a FDM-based (fusion deposition modeling) Makerbot 2X, but it was quickly determined that a SLA (stereolithography) printer would be required to obtain the necessary resolution. Good results have been obtained using an Objet 30 and Formlabs printers. A variety of Formlabs resins, including Rigid, Grey, Clear, High Temperature, Tough and Dental SG were simultaneously  $\mu$ CT imaged to determine whether any particular resin had different imaging parameters such higher or lower intensity. No significant

differences were observed; therefore, all subsequent printing was performed with standard Grey resin as it is the least expensive. Annulus clamps (but likely not PM hardware, due to their small, complex geometry) are also suitable for CNC machining.

In addition to annular geometry, several important features are modeled into the clamps. First, the hole pattern must remain invariant across all valves so that it remains compatible with the imaging system (section 2.3.1). The edge of the ventricular clamp half, closest to the CT, has a generous chamfer to minimize the chances of interference as well as improving visibility during biomechanical loading (section 2.5.1). A set of cone-shaped holes are included on the exterior flat faces. These serve as registration points for subsequent image analysis (section 2.4.1). Finally, each clamp carries a unique identifier number depressed into the above mentioned flat face.

## **2.3 Imaging**

The mitral valve has been successfully imaged by several groups using a variety of imaging modalities, including MRI, uCT, stereotactic X-ray, optical, etc. [28,31-35] . The choice of imaging methodology is driven by factors such as *in vivo* vs. *in vitro*, desired resolution, permissible sample volume and the availability and logistics of imaging equipment.

### ***2.3.1 Imaging System***

At the outset of this work, a collaboration was ongoing with the National Center for Toxicology Research (NCTR) in Jefferson Arkansas. Available at NCTR was a Bruker BioSpec 70/30AS MRI (Bruker, Billerica, MA) with a 72 mm bore diameter and 7T field strength. A preliminary,

exploratory scan had already been performed on a partial mitral valve with good results. Design of the initial imaging apparatus, shown in Figure 5a, was performed specifically with this machine in mind. This system, as well as how the custom-made mounting hardware interfaces with it, has been previously described in **Stephens, Plos One** [31]. In summary, the valve is held by a physiologically-shaped annulus clamp and papillary muscle holder (section 2.2) that are mounted within the clear acrylic case. The case itself has two separate chambers, permitting the generation of trans-mitral pressurization for valve closure.

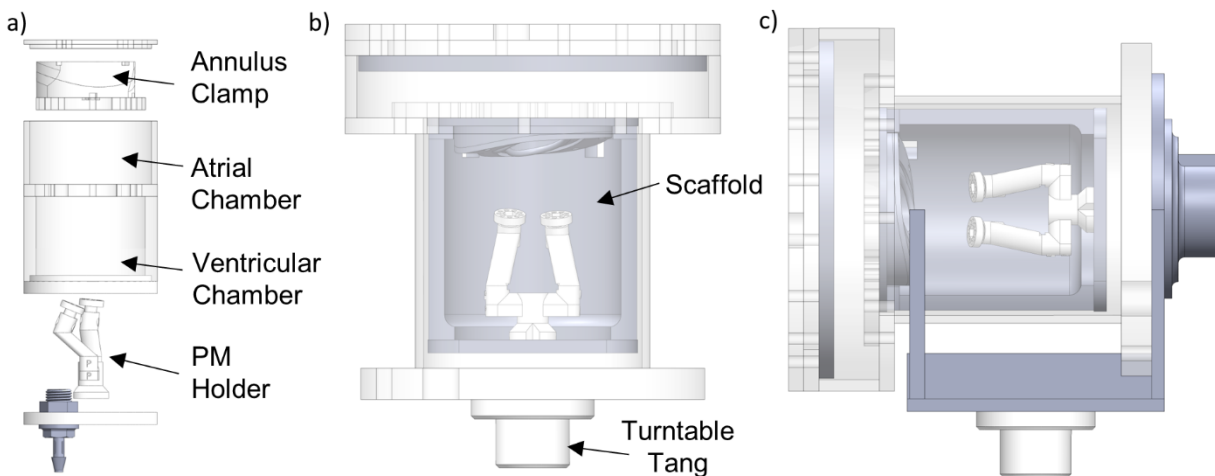


**Figure 5** – a) Previously reported imaging system (developed for MRI), b) new  $\mu$ CT imaging system c) new system with closed-scanning adapter

Tissue desiccation during scanning is a potential issue as it not only can lead to sample movement, spoiling the imagery, but altering tissue mechanics which is critical for subsequent analysis. When imaging tissues with MRI a liquid perfluoropolyether (PFPE) oil is commonly used, which reduces/eliminates desiccation. Commonly used PFPE oils for MRI include Fomblin and GeminYe. These oils are especially suitable to MRI imaging because they lack hydrogen atoms, whose nucleus is composed of a single proton. Given that MRI imaging relies upon proton spin alignment, hydrogen-bearing fluid mediums appear opaque. Additionally, these oils

have a similar magnetic susceptibility to that of tissue, reducing image artifacts. Despite their excellent suitability for MRI tissue imaging, these oils, which are primarily used as an aerospace lubricant, are expensive and difficult to work with. Leak-proofing, particularly within a pressurized system, is difficult and any leaks/spills must be cleaned with special solvents. These oils frequently exceed \$300/Kg, with the solvents being somewhat expensive as well. Due to prolonged exposure to un-fixed tissue, any oil used for imaging develops a strong smell and is not reused.

When the University of Arkansas acquired a Nikon X TH 225 ST (Nikon, Tokyo, Japan) micro-computed tomography ( $\mu$ CT) scanner, exploratory scans were made (using the same imaging apparatus) and found to be comparable in quality to those obtain from MRI. Scan times were much reduced, from 30 hours to approximately 15 minutes. Example 3D renders generated from MRI and  $\mu$ CT scans, illustrating the comparable quality, may be seen in Figure 6. Logistically,  $\mu$ CT proved simpler as well due to the very close proximity. Desiccation was once again a concern however, as  $\mu$ CT/CT scanning is nearly always done in air. This is due to the x-ray nature of CT imagery, where x-ray absorption, the main determinant in image intensity, is primarily determined by density. Given that tissue has similar density to most fluids, little contrast is therefore achieved between sample and background. It was nevertheless desired to image within a fluid medium so as to eliminate desiccation as well as non-physiological effects, such as tissue “bunching” that has been observed in air. To this end, a DiceCT staining process was implemented (detailed in 2.3.2).

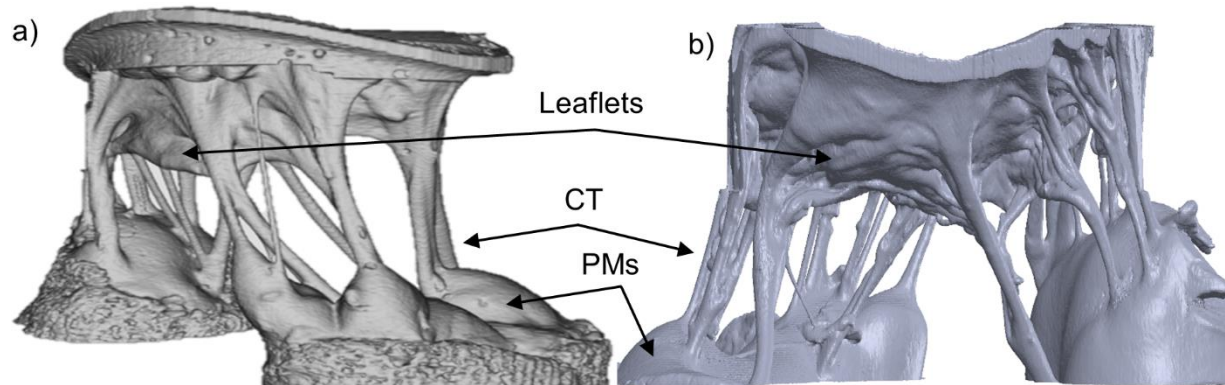


**Figure 6** – Example 3D renders of data obtained from a) MRI and b)  $\mu$ CT [31,33]. Voxel resolution is approximately 80 and 38-micron respectively.

Due to the shift from MRI to  $\mu$ CT imaging, several modifications were made to the design of the imaging apparatus discussed above. The final imaging apparatus is shown in Figure 5c. Firstly, all metals were removed from the apparatus as these cause significant starburst-like artifacts within the images. The brass nuts and bolts used in the MRI apparatus were swapped for plastic. To ensure sufficient strength, the size of the fasteners was also increased from M3 to #10-32 threads where possible. Similarly, it is necessary to separate the system from the scanner's metal turntable. For unmounted (usually exploratory or preliminary) scans, or scans where the full imaging system is not used, a block of Styrofoam can be placed between the sample and turntable. Styrofoam is nearly invisible to x-ray due to its low density, and therefore separates the sample from turntable without appearing in the subsequent images. For scans where the full imaging apparatus is required, the turntable can be removed entirely, and the apparatus mounted directly to the drive by a plastic tang that matches the geometry of the turntable tang. Given that the tang is mounted along the axis of the cylindrical apparatus, direct mounting also makes it easier to ensure that it is centered and will not collide with the detector. This permits it to be positioned closer to the detector, maximizing resolution. Unlike the original MRI imaging

system, valves may be fully mounted before insertion. The previously described system required, due to its limited size, that the PM's be mounted within the case; this was extremely tedious. The new system mounts the annulus clamp and PM holder onto a scaffold structure that inserts and secures within the system, greatly simplifying and expediting mounting. Many other quality-of-life improvements were also made, such as the larger atrial chamber diameter, that makes it significantly easier/quicker to mount valves within. Finally, an adapter was produced to place the system in a horizontal configuration (figure 5c), which is beneficial for closed-valve scanning and fiducial localization (section 2.3.4 and 2.4.2).

### ***2.3.2 DiceCT Staining***

Diffusible iodine-based contrast-enhanced computed tomography (DiceCT), a staining technique for increasing the contrast of soft tissues under x-ray, was investigated as a means to more easily discern mitral valves from their fluid background. DiceCT utilizes an iodine-based bath of Lugol's solution to stain soft tissues, increasing their radiopacity. A relatively new technique, DiceCT is generally utilized to more easily distinguish differing tissues as the stain uptake varies by tissue. Samples are usually stained throughout, ensuring the more central regions become adequately exposed. For the purposes of mitral valve imaging, no tissue-tissue discernment is necessary as the important structures (CT, leaflets, etc) are easily identified by geometry. Additionally, the valve's surfaces are the primary regions of interest, eliminating the need to ensure thorough, homogenous staining. This work has been previously published in **Experimental Mechanics, Stephens** [33].

In summary, various staining times and concentrations of Lugol's Solution were evaluated to determine an optimum tissue-background contrast while minimizing artifacts. Excised mitral



valves were immersed within Lugol's solution and gently agitated to ensure thorough exposure. Staining solution concentrations considered ranged from 0.5 to 2.85 % weight/volume, with stain times from 0.5 to 5.5 hours. All valves were scanned identically following staining and the intensities of the leaflets manually measured in ImageJ. Additionally, several fluids, including deionized water, 90% ethanol, glycerin and olive oil, were evaluated to determine whether the choice of fluid had an effect. It was determined, that of those evaluated, olive oil had the greatest contrast. When imaged in olive oil, DiceCT stained mitral valves were clearly distinguishable from the background. Several example slice-images, each at differing stain parameters, are shown in Figure 7. A moderate staining protocol was selected as ideal; aggressive staining (either through high concentration and/or exposure time) can lead to the generation of artifacts.

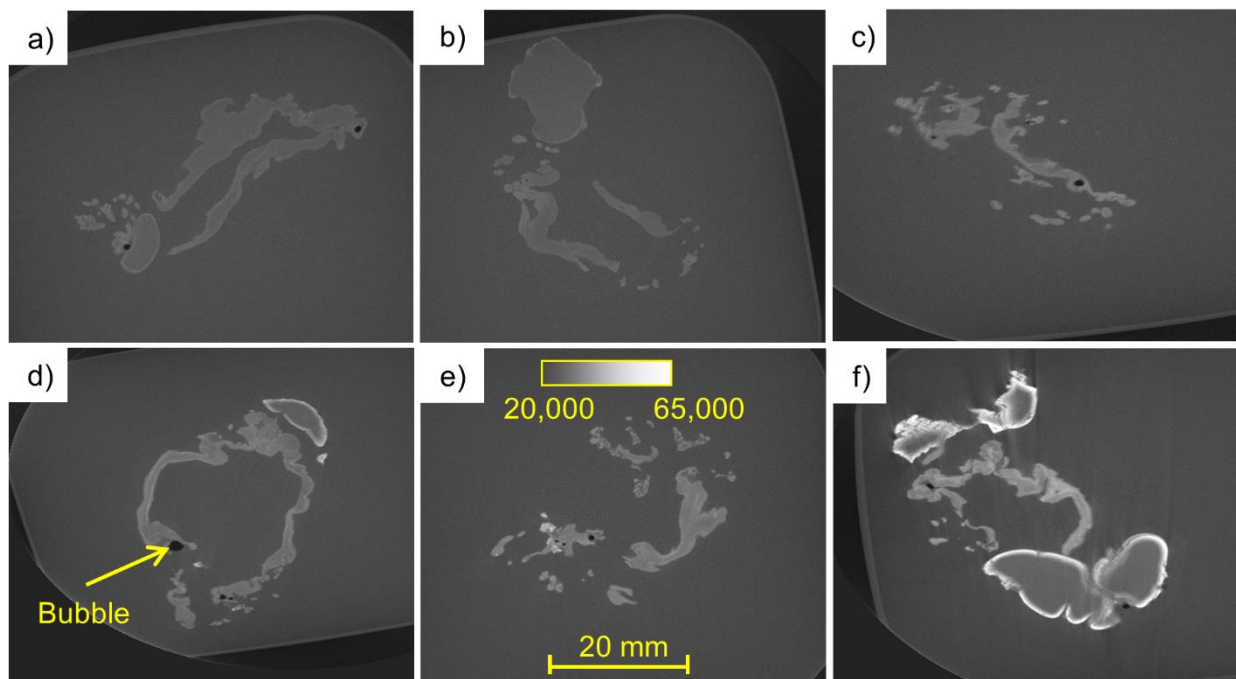


**Figure 7** –Example images from staining study. All slices intersect approximately the same anatomical structures on each valve. All valves were scanned in *Olea europaea* oil with the following staining parameters: (a) 0.5 h @ 0.5% w/v, (b) 3.5 h @ 0.5% w/v, (c) 0.5 h @ 1.28% w/v, (d) 3.5 h @ 1.28% w/v, (e) 0.5 h @ 2.85% w/v and (f) 3.5 h @ 2.85% [33]

### ***2.3.3 Fiducial Markers***

Registration of opened and closed valve scans requires the placement and subsequent localization of multiple fiducial markers. Fiducial markers come in a variety of sizes, shapes and materials, but all generally serve to aid in the localization of regions of interest. Radiopaque markers, or those that appear as bright regions in x-ray imaging, are ubiquitous within CT and  $\mu$ CT imaging. Some are available commercially, both for clinical and research applications, but many researchers use “home brewed” options. Specially shaped markers, such as tetrahedra, can permit measurement of orientation changes in addition to centroid displacement, though this adds additional complexity to the analysis. Within soft tissue biomechanical studies, markers must not only be clearly visible under x-ray but also should be as small as possible to minimize their effects upon their carrier tissue.

While many markers have been used historically, they are generally reported upon in isolation with little/no comparison to other materials. Prior work has compared various materials specifically for use with mitral valve imaging and found the best contrast was achieved by a marker made from montmorillonite clay desiccant [32]. Test scans with our setup and equipment however showed somewhat lackluster contrast, with DiceCT scans being very poor due to the desiccant absorbing staining solution. A study was therefore performed to find a suitable material that showed good marker-tissue contrast when imaged both in air and in oil following DiceCT staining. Materials considered included: tantalum, 24K gold, glass, alumina, 316L stainless steel, lead, Delrin plastic and desiccant. Tantalum and gold were selected as they are commonly used in clinical settings. Markers were adhered to mitral valves by first dredging them in CA glue and pressing against the anterior leaflet with tweezers until bonded. Several markers were thusly adhered to a single valve to permit their direct comparison in the resulting  $\mu$ CT imagery. All

markers were scanned under identical conditions. The results of this study have been published in **Stephens, Alumina, ExpMech** [36]. In summary, excellent results were obtained using alumina (aluminum oxide) fiducial markers. Alumina showed excellent radiopacity with minimal artifact generation when imaged both in air and olive oil following DiceCT staining of the tissue. The alumina was sourced as an industrial abrasion media, available in a range of sizes. The above study utilized 500 micron-diameter balls that also showed good sphericity, an important characteristic to facilitate straight-forward localization. In addition to the more conventional use in post-reconstruction analysis, the alumina markers were also clearly visible in unreconstructed projection images. Example reconstructed slices showing alumina and several other materials may be seen in Figure 8.

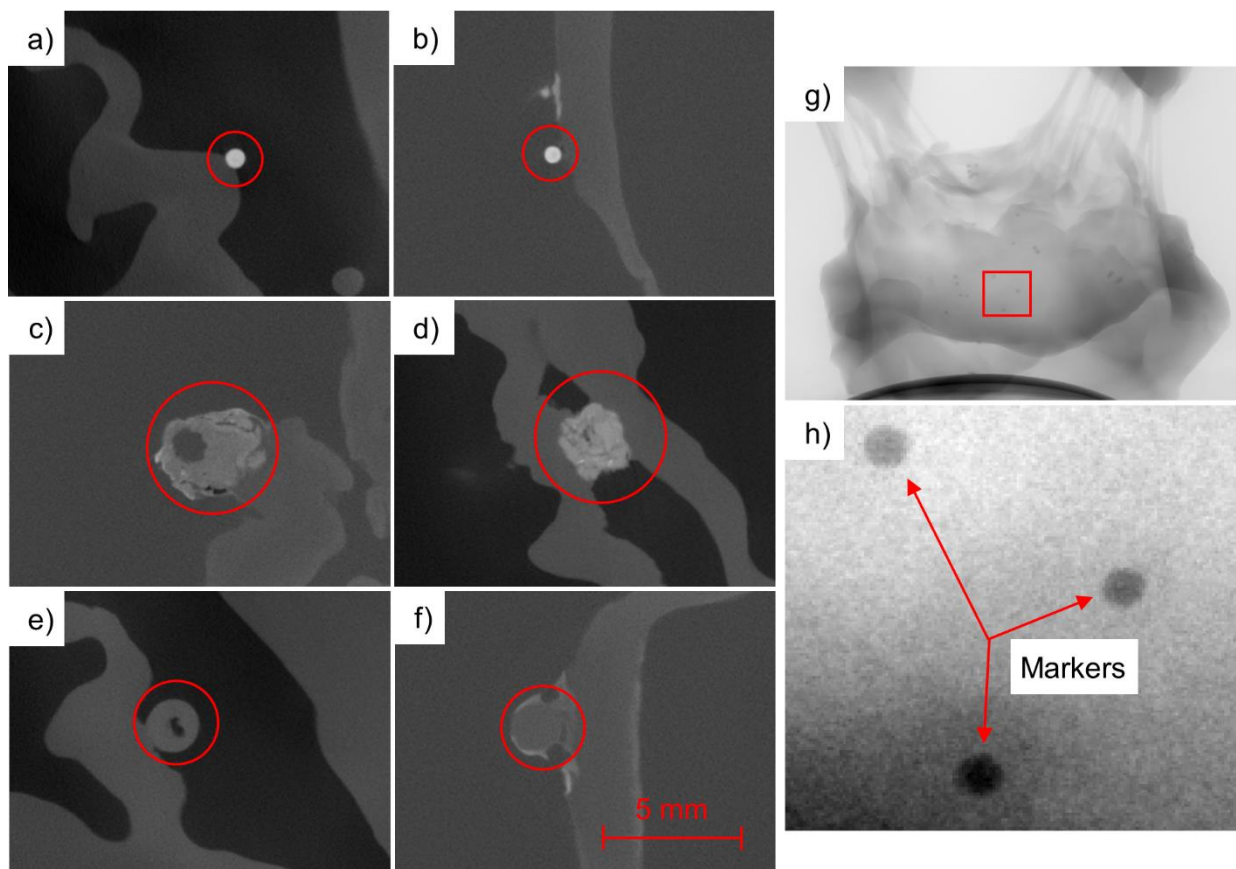


**Figure 8** – Example marker images showing a) Alumina, b) Alumina – DiceCT, c) Desiccant, d) Desiccant – DiceCT, e) Delrin, f) Delrin – DiceCT, g) unreconstructed projection with alumina and h) inset of g) [36]

#### ***2.3.4 Closed-Valve Imaging***

As previously mentioned, valve closure requires the establishment of trans-mitral pressure.

Given the complexities with leak proofing a pressurized container (regardless of fluid), it was decided to close valves using pressurized air. Any small (liquid) fluid leak would prove extremely problematic within the delicate and expensive  $\mu$ CT scanner, whereas air leaks can be tolerated. To minimize tissue desiccation, which has been previously discussed to be problematic, closed-valve imaging is kept to as short a duration as possible. A method, detailed later in section 2.4.3, was developed whereby a small, quick set of projection images may be utilized to localize fiducial markers, permitting registration.

A pressurization system, illustrated in Figure 9, was developed whereby a previously charged air tank delivers compressed air to the ventricular chamber of the imaging system. An in-line regulator ensures physiologically appropriate pressure is delivered to the valve. A 4.54 L (1 gallon) tank was selected to provide sufficient capacity to maintain closure during the short closed-valve scans as well as to fit within the  $\mu$ CT scanner cabinet, underneath the x-ray source. A thin, soft latex tube is used to connect the solenoid output to the ventricular chamber to minimize the mechanical forces (which would likely cause sample movement) imparted to the rotating imaging apparatus. This tube is additionally strain-relieved by a connection point to the interior of the scanner cabinet. The entire pressurization system fits within the scanner cabinet. The tank pressure gauge is rotated such that its face is visible through the scanner door window.

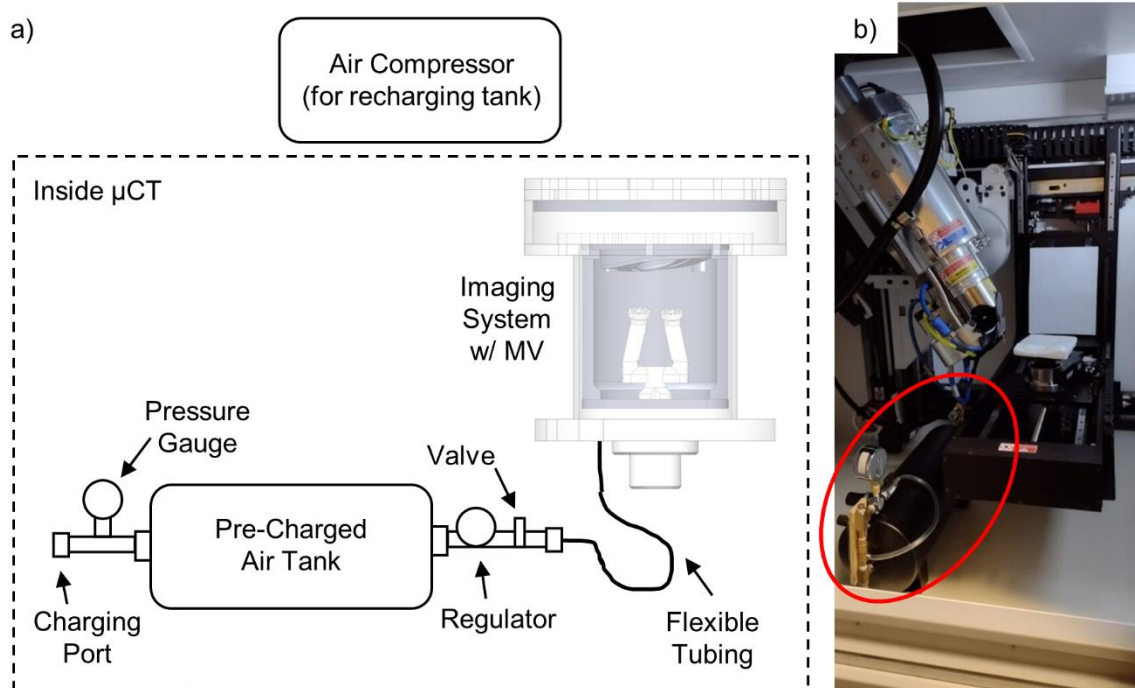


**Figure 9** – Pressurization system for closed valve scanning; a) schematic view of components and b) system installed within  $\mu$ CT scanner cabinet

For closed, systolic-configuration imaging, a separate adapter (section 2.3.1) is used to rotate the imaging apparatus by 90 degrees to better resolve the valve’s fiducial markers (section 2.3.3). The adapter and imaging apparatus are shown in Figure 5c. This adapter utilizes an identical plastic tang to mount to the turntable receptacle. For systolic imaging, the imaging apparatus is first drained of oil and then attached to the adapter by means of a tang receiver. The adapter is mounted within the scanner and the pressurization system attached through a Luer port on the ventricular side of the imaging apparatus.

## 2.4 Data Analysis

$\mu$ CT imaging generates an image stack of raw projection images. Scrolling through this stack shows the sample and turntable rotating and can be useful for checking for mid-scan sample

movement, which should be minimized. Projections are also useful for evaluation of stain leaching for scans utilizing DiceCT techniques. For more practical use, these projection images are reconstructed to obtain a more conventional stack of slice images that “cut” through the sample at differing heights. This reconstruction is generally performed by  $\mu$ CT staff. A brief summary of reconstruction is as follows: Raw projection TIF images are sent from the  $\mu$ CT scanner to a separate reconstruction workstation. These projections are loaded into CT Pro 3D (Nikon), where the center of rotation, beam hardening correction, enhancements, and volume size parameters are created. This information is then sent to CT Agent (Nikon) which produces a VGL file, which is then used by VGStudio MAX (Volume Graphics GmbH, Heidelberg, Germany) to perform histogram scaling. The projection images are then reconstructed into a z-axis-aligned stack of slice images. Metadata files are also generated which detail scanner parameters such as beam current, energy, exposure time, voxel size, etc.

It should be noted that histogram scaling performed during the reconstruction process will affect the intensities of the final reconstructed stack; if comparative studies are to be performed, in which multiple scans will be quantitatively compared, these scaling values should be noted and kept constant. The projection stack is not always retained for every scan as it is often not useful to the scan objectives and can be quite large, often around 20 Gb per scan. Projections and/or reconstruction volume data (illustrated in Figure 10) are stored online by  $\mu$ CT staff for backup purposes. Following reconstruction, the slice stack and associated meta-data is transferred via USB and stored for subsequent analysis. The image size and number of images is dependent upon the sample size/resolution and crop settings, but generally is in the neighborhood of 5 Gb per scan. Final voxel size varies and is a function of scan setup, though the scans routinely done throughout this work were in the 30-35-micron range.

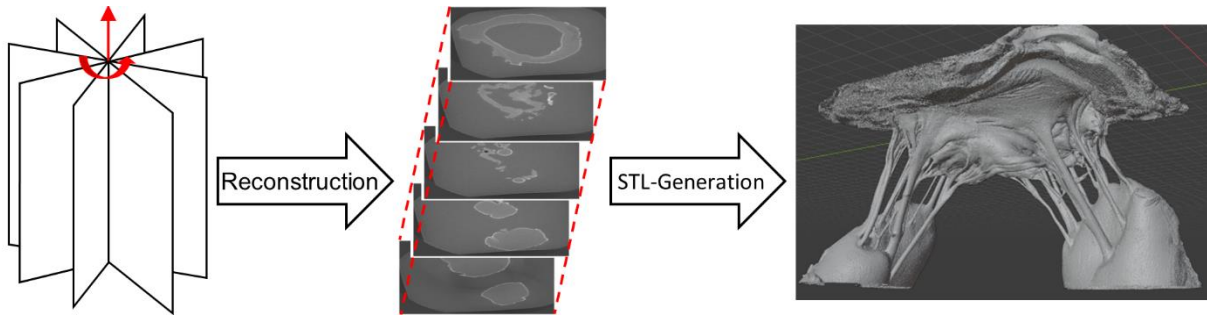


**Figure 10** - Illustration of the projection-to-STL generation process

### ***2.4.1 Hardware Subtraction***

The reconstructed images show not only the valve but also the mounting hardware and imaging case, along with the fluid background if applicable. For later purposes of providing geometry input for FEA simulation, all non-valve areas need to be removed from the imagery. Frequently, such unwanted areas are removed using intensity-based methods such as Otsu’s Method or Watershed segmentation. If sufficient contrast is present between the tissue and adjoining areas then these methods may be employed, as was the case with our previously published MRI data, where the valve was separated from a background of PFPE oil by intensity thresholding [31]. If the contrast is low however, which is generally the case when comparing tissue and mounting hardware, then these methods are unsuitable as they may leave unwanted areas, or more seriously, erroneously remove portions of tissue.

The fact that mounting hardware is custom tailored for each valve, with the geometry therefore being precisely known, permits the removal of hardware from the image stack based upon this known geometry rather than by intensity. An algorithm was developed to utilize this known-geometry; a manuscript detailing these methods is currently under review. A summary of the methodology is illustrated in Figure 11, with more in-depth discussion following.

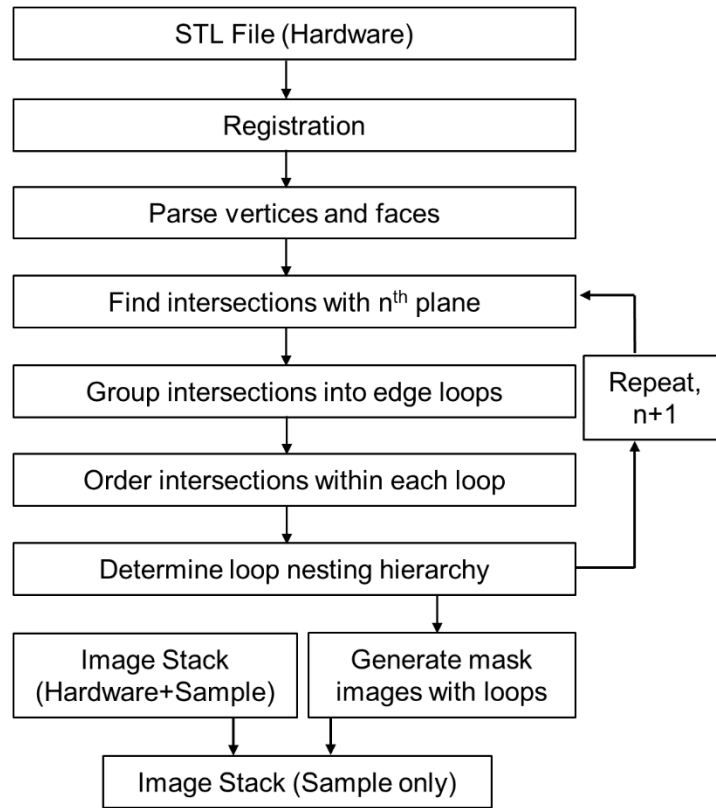


**Figure 11** – Flowchart representation of the major operations within the hardware subtraction algorithm

Hardware geometry is input in the form of a binary STL (standard tessellation language) file, obtainable in a variety of ways, most commonly as a direct export from a CAD (computer aided drawing) model or from a 3D scan of the hardware. The STL format represents object surfaces as a mesh of triangular facets, with the vertices bounding each facet listed as coordinate points within the STL file itself, along with the unit vectors for the facet’s normal vector. In addition to selecting the intended STL file, the user also provides several inputs including the locations of three (or more) fiducial points. Fiducial points are ideally modeled into the hardware itself in such a way as to allow easy, precise identification. All user inputs are obtained through a graphical user interface.



A rigid-body transformation is first conducted so as to register the three (or more) hardware fiducial points (whose positions with respect to one another is known) with their positions within the image stack. The centroid of the fiducial points is calculated, and the necessary rotation matrix  $R$  is found by singular value decomposition (SVD). The translation matrix  $T$  is then determined by the required translation to align the image stack points and the rotated hardware points. This transform ( $R$  and  $T$  matrices) is applied to all STL vertex points to properly register the STL to the orientation of hardware within the image stack.

A plane is constructed such that it is coincident with the bottom-most image that shows hardware. The transformed vertex coordinates are parsed into separate faces and associated edges. These faces are evaluated to determine which ones intersect or cross the plane by computation of the dot product of the plane's normal vector and a vector from an arbitrary point on the plane to each face vertex. For each face that crosses the plane, all intersection points are found by determining the intersections between the plane and the three face edges. All intersections with the plane, for all STL faces, are compiled into an array. An example of these intersections for a mitral clamp image slice is shown in Figure 12c, as well as examples for each of the following steps.

The planar intersections trace out the edges of the model formed by a cross sectional cut taken at the plane. In the event that the hardware element has several branches or internal features, such as holes, then the multiple edges will be represented by the points within the intersections array. In order to separate the intersection points into individual edge "loops", a connectivity-thresholding approach is employed. An arbitrary intersection point is selected and the distance to all other points is computed. All points within a preset threshold distance are considered to be within the same loop and are added to a new loop array. The process is repeated using the next of

these new points as the base point for finding the distance to all remaining intersections. Once no additional intersection points are found within the threshold distance, then a new loop array is started using one of the remaining, unassigned intersections as the basepoint. By this process all intersection points are assigned to loops with each loop array representing a different edge (Figure 12d).

The grouped intersections are next ordered within the individual loop arrays such that they would present the smooth, cross-sectional outline of the model if connected in a connect-the-dots manner (Figure 12 e and f). An arbitrary point within each loop is selected as the starting point. The distance from this point to all others within the loop array is determined and the nearest neighbor is selected as the next point in the ordered sequence. The distance from the second point to all others is similarly found to determine the third point. After repeating for all subsequent points, the loop is closed by returning to the starting point. An alternative solution to this “nearest neighbor” approach is a Traveling Salesman Solver, though several implementations have shown issues with uniqueness and execution time.

Once all loop arrays have been ordered appropriately, it must be determined, for each loop, whether it represents an interior or an exterior edge. An interior edge could, for example, be formed by a hole or cavity. A single point is selected from each loop and checked whether it is inside each of the other loops using Matlab’s `inpolygon` function (Mathworks, Natick, MA). If the point is interior to any of the other loops then it is part of an interior loop, otherwise it is exterior.

The now appropriately ordered and looped intersection points are used to generate polygonal masks that are applied to a template file, equal in size and resolution to those of the image stack. For exterior edge polygons, the bounded region is flood filled white (assuming a white object against black background for the image stack) while interior edge polygons are filled black. The

resulting mask is saved as a new file in a separate directory with consistent numbering as the original stack. Pixel-wise multiplication between the mask images with their respective data images leaves only the region(s) of interest, without the hardware.

The above procedure is repeated for a new image plane, offset from the first by the data image stack inter-image spacing. This continues until the image plane height matches the uppermost image which displays the hardware to be removed. By this process, analysis is conducted on an image-by-image basis, without the need to read to file all images simultaneously.

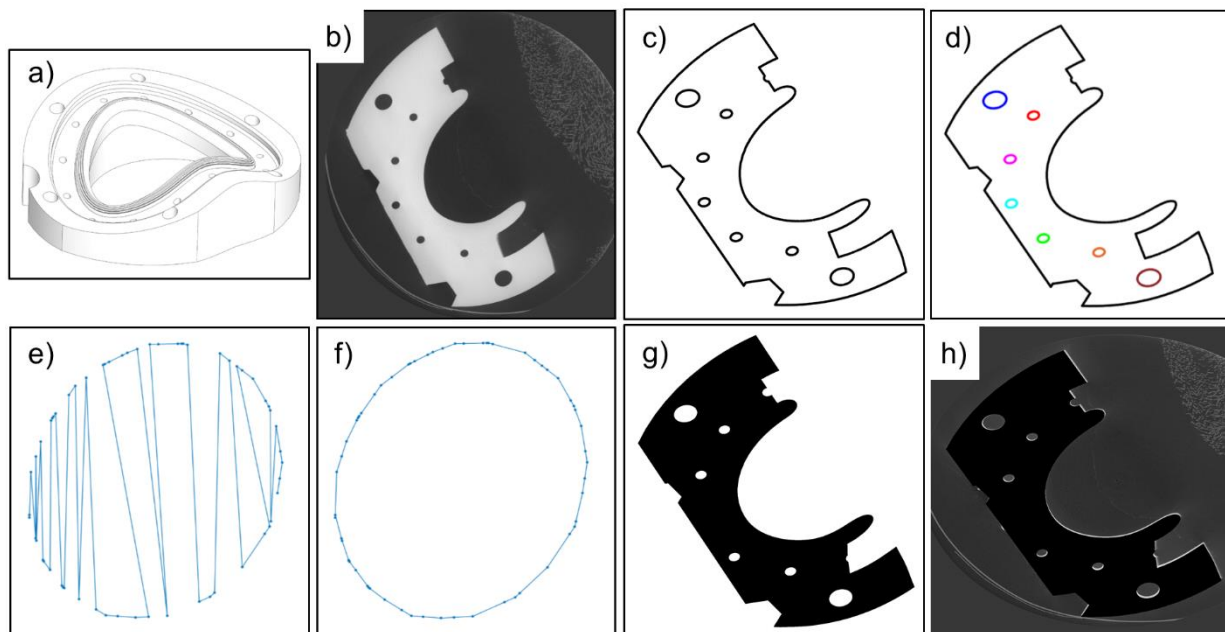


**Figure 12** – Render of a) mitral clamp half and b) single slice image from  $\mu$ CT scan. Example outputs from intermediate steps within subtraction algorithm showing c) intersections with plane, d) color-coded loops, e) example of unordered loop, f) example of ordered loop, g) final mask and h) result of pixel-wise multiplication of mask with initial image

### ***2.4.2 Fiducial Localization***

Registration of open and closed valve scans requires the accurate localization of fiducial markers. Markers may easily be localized in the open scan due to its superior resolution. This can

be accomplished by inspection of the STL model, manually determining coordinates at/near each fiducial centroid. Many softwares, such as Blender, permit inspection and measurement of STL files. Alternatively, fiducials may be localized directly from the reconstructed image stack. All fiducial coordinates are taken relative to reference points within the imaging case.

Localization of fiducials within the much quicker, closed valve is more challenging. All other variables kept constant, the number of projection images obtained is proportional to overall scan time. As scan times are intentionally minimized for the air-pressure closed valve, the total projection count is thereby limited. The quality of reconstruction, through methods such as filtered back projection, is linked to projection count. Localization from STL or slice stack, both of which require reconstruction, are thus not possible. Instead, the raw projection images are utilized.

The rotation between projections is accurately known due to the  $\mu$ CT sample turntable being stepper motor driven. This may be the case for other imaging systems, such as c-arm and other cone-beam CT. Provided that fiducial markers are visible within projections (as established in 2.3.3), successive images of known angular displacement may be utilized to triangulate fiducials. Ray tracing is employed, where linear rays are followed from an idealized point source, through each fiducial marker, and to a flat detector panel. The detector/image displacements are measured between successive projections that are separated by a known angular rotation. Fiducial coordinates may then be calculated by utilizing known geometry of the scanning equipment. Full mathematical details may be found in Appendix B.

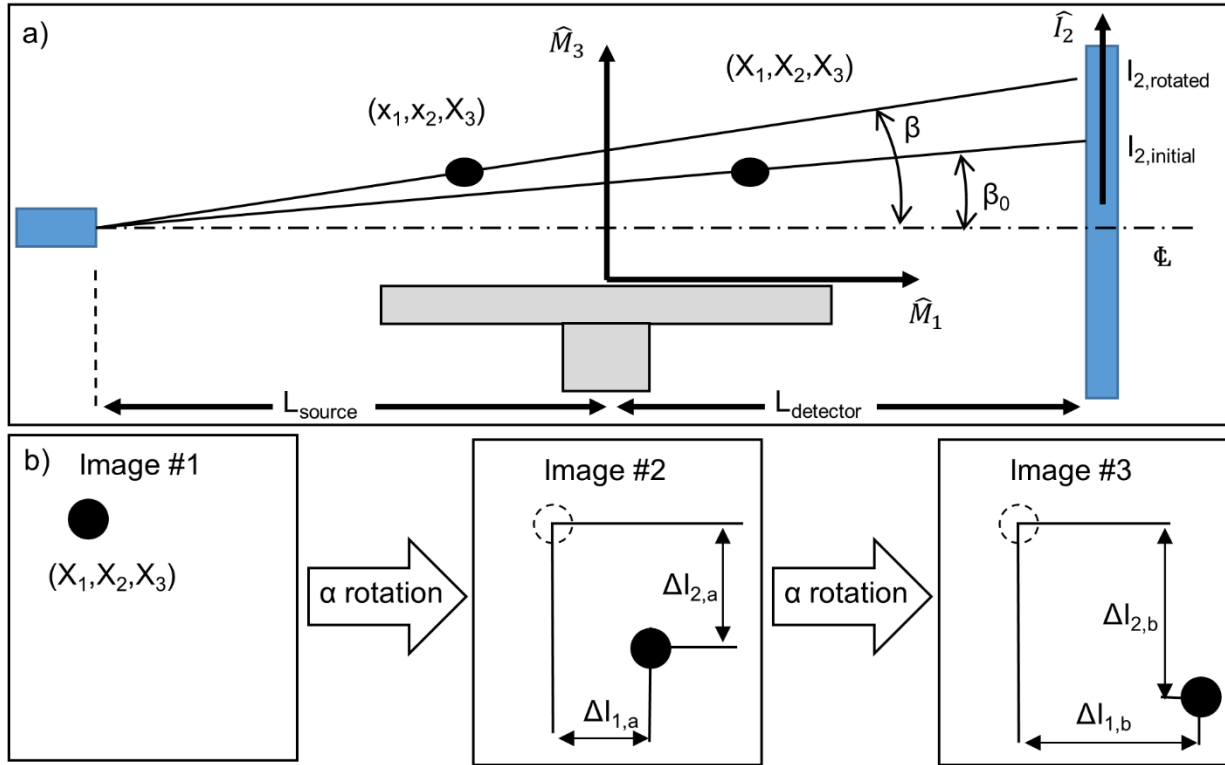


**Figure 13** – Schematic illustration of fiducial localization technique; a) side view of  $\mu$ CT scanning setup and fiducial displacement, b) inter-image fiducial movement and dimension definitions

To test the localization accuracy, a virtual scanner setup was constructed using Solidworks. A triangular sample was rotated about a turntable axis and rays projected from a point source through the vertices of the sample. These rays were projected onto a detector plane and the locations of the intersections found. These “images” were obtained for three angular positions of the sample. The full virtual setup is shown in Figure 14.

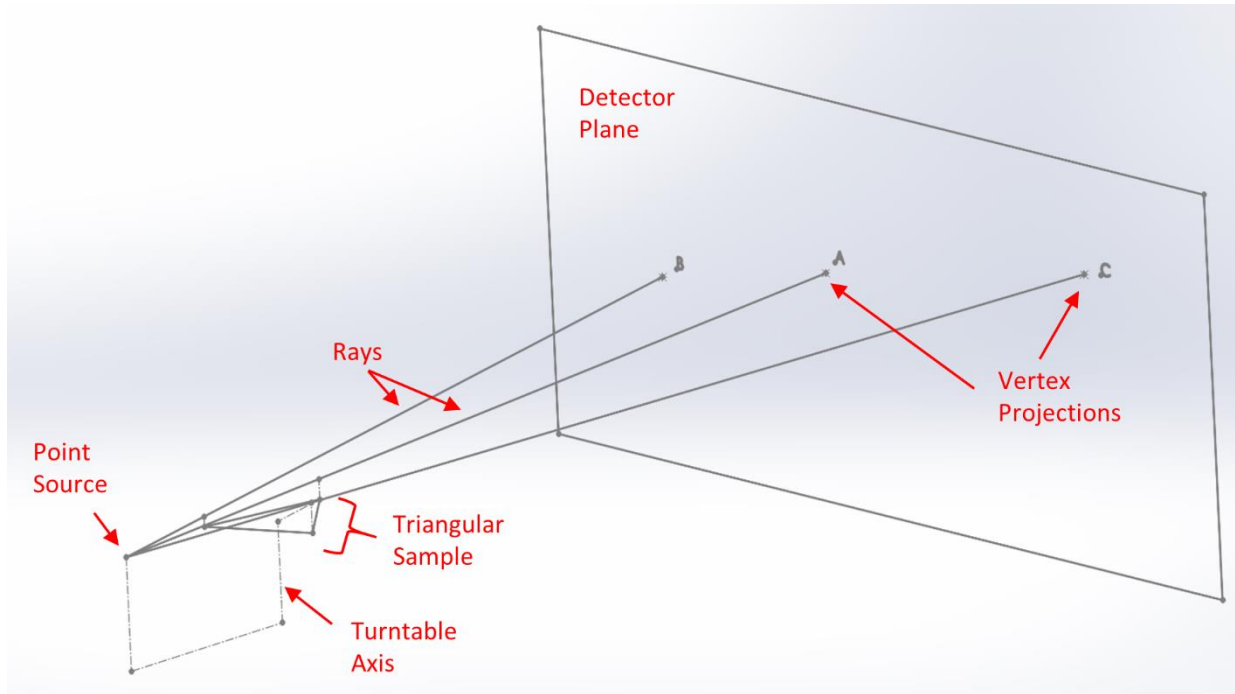


**Figure 14** – Setup of Solidworks virtual scanner. The triangular sample is rotated about the turntable axis.

For the virtual validation, “pixel” locations were non-discreet but rather formed a continuum; fiducial pixel locations were measured to five decimals precision. To evaluate the accuracy of the localized fiducial coordinates against their known locations, the edge lengths of the triangle formed by the three fiducials were computed. Actual and calculated edge lengths are presented in Table 1, along with the percentage error between them.

Edge	Actual (mm)	Calculated (mm)	% Error
AB	33.7018	33.7025	0.002216
AC	28.2907	28.2893	-0.00487
BC	28.0315	28.0315	-0.000018

Table 1 – Calculated and actual edge lengths for virtual validation

A second validation was conducted, in which a 3D printed sample with easily identifiable, known-location features was scanned. Three conical vertices, at differing heights to facilitate

clear identification, represent fiducial markers. The sample, shown in Figure 15a, was printed using a Form 2 resin-based 3D printer. Standard grey resin was used with a layer resolution of 25 microns. Scan data was obtained using a 145 KV beam energy and 155  $\mu$ A beam current. A reflection head was utilized no filter. Resultant projection images had a resolution of 25 microns. Direct identification of the vertices of the 3D printed sample (within the  $\mu$ CT projection images) wasn't possible as the vertices were "washed out" (Figure 15b). Therefore, an edge-fitting approach was employed in which lines were fit to the triangular projection of the point and their intersection found, giving the vertex location. Through a custom-built Matlab GUI (graphical user interface), the user is prompted to select a series of points, shown as red dots in Figure 15c. Pairs of user-selected points then define lines whose intersections are found. A bisector/diameter is also calculated to evaluate foreshortening effects.

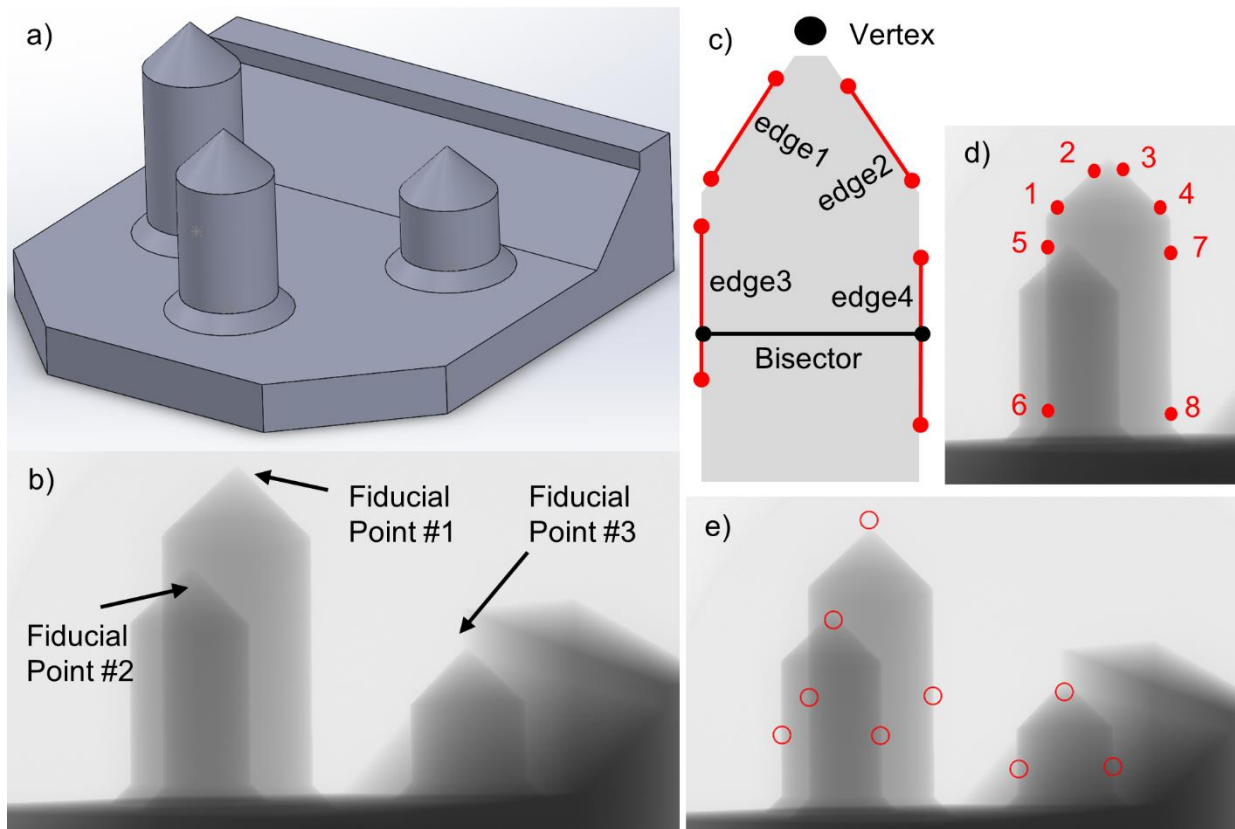


**Figure 15** – Localization phantom shown in a) Solidworks rendering and b) projection image. Vertex fitting scheme is illustrated in c) along with d) user inputs and e) fitted vertices and bisector endpoints

Edge lengths for the triangle formed by the fiducial points were similarly computed for the 3D printed sample, both from known as well as localized coordinates. These lengths, along with the percent errors, are given in Table 2.

Edge	Actual (mm)	Calculated (mm)	% Error
AB	17.56	17.88	1.781
AC	26.63	27.36	2.771
BC	22.70	23.26	2.445

Table 2 - Calculated and actual edge lengths for physical, scanned validation

## 2.5 Biomechanics

### 2.5.1 Vacuum Valve Closure

Given that valves close as a result of a trans-valvular pressure difference, the natural method to close explanted valves is to isolate each side in a separate pressure vessel. This method has indeed been employed by a variety of research groups. Experience with mounting and manipulating valves within the above-described imaging apparatus has shown the difficulty of operating within small, sealed vessels. While the atrial and ventricular pressures that together generate an appropriate trans-mitral pressure are generally thought of as positive, the valve itself imposes no such limitations. An apparatus was constructed to apply vacuum pressure to the atrial side of the valve, permitting the ventricular side, with highly relevant sub-valvular apparatus, to remain open to the atmosphere. Atrial vacuum pressure was controlled to maintain an appropriate trans-mitral pressure. The construction and demonstration of the vacuum-closure apparatus, illustrated in Figure 16, has been previously described in **JCTR, Stephens** [37]. In



summary, an asymmetric u-shaped chamber was created from clear, ½ inch thick acrylic sheets. The chamber was filled with water and vacuum pressure was introduced through a port connected to a vacuum chamber and pump. An orifice is covered by the mounted valve, transmitting vacuum pressure through the water to the valve’s atrial side. The ventricular side is subject to atmospheric pressure, with a small amount of water to prevent desiccation. To validate valve closure, total PM force and regurgitant flow rate were measured and found to be within clinically normal ranges. This open, unrestricted ventricular access vastly improves the ease of instrumentation and manipulation of sub-valvular structures. For instance, chordal force gauges may be more easily positioned without the concern for waterproofing, either the gauges themselves for the cable routing through an otherwise sealed vessel. Optical measurements of the chordal network are more feasible without the often distorting effects of vessel walls.

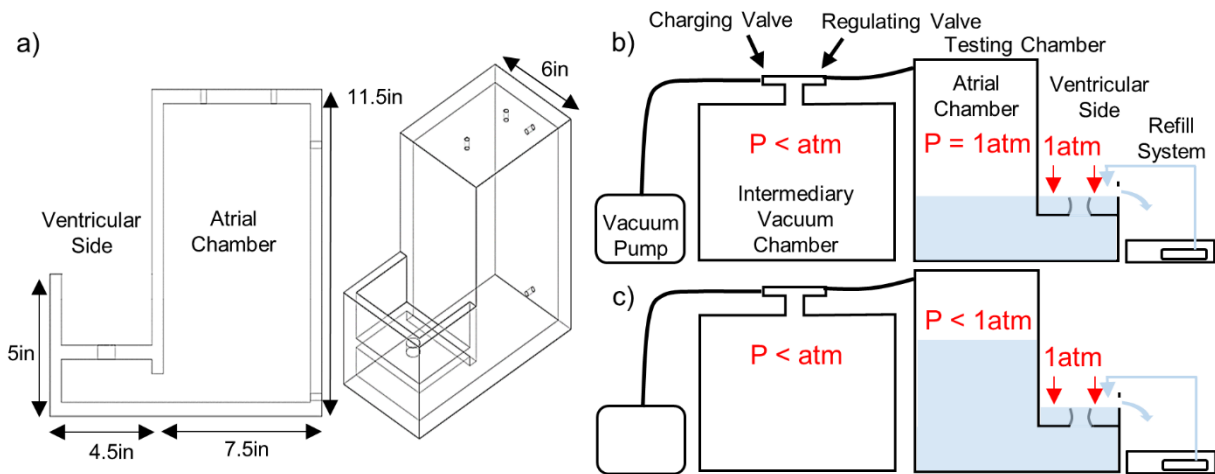


**Figure 16** – Vacuum closure system a) Schematic representations of system b) open-valve and c) closed valve configurations

### 2.5.2 Chordal Force Gauges

Previous efforts to measure chordal forces have commonly utilized the classic c-shaped stain gauge. This configuration places a pair of strain gauges on opposing sides of a c-shaped frame,

which when subject to tensile loading, produces a measurable change in gauge resistance. Such gauges have been used both *in vivo* and *in vitro* with good results. One shortcoming of these force measurement devices, however, is that they frequently occupy a relatively large space within the congested chordal network. Should the frame interfere with neighboring chords it may alter the native force balance. Additionally, the conventional c-shaped frame “replaces” a good deal of length from the chord it is mounted along. As the Young’s modulus differs for the chord and the frame, this will also alter the native force balance by changing that chord’s overall strain. It is for these reasons, viewed particularly through the lens of unobstructed ventricular access, that a cantilever-based strain gauge frame was designed.

The frame, shown in Figure 17a, has two cantilever arms that each carry two strain gauges with one in compression and one in tension. This gives a total of four gauges to be mounted per frame, thereby permitting a full Wheatstone-bridge to be used, giving increased signal over the half Wheatstone-bridge that is common to c-gauges. The frame itself is long rather than tall, extending outwards from the chordal network comparatively far, yet also minimizing the length of chord altered. In many sealed pressurization vessels, and certainly *in vivo*, such long gauges may be problematic, but not here due to the open ventricular access previously discussed. Micro strain gauges are attached near the rear of the arms, where the strain is maximized due to bending. Wires for signal and excitation are routed through a channel for strain relief on the electrical connections. The frame’s dimensions were determined iteratively through Solidworks FEA simulation to obtain a target strain of approximately 10 millistrain. A Formlabs Form 2 3D printer with standard grey resin was used to produce the frames in two halves for ease of strain gauge application on the inner faces. A layer resolution of 25-micron was used to fully resolve

the frame's small details. Following gauge application and wire routing, the two halves are bonded together using cyanoacrylate adhesive (CA).

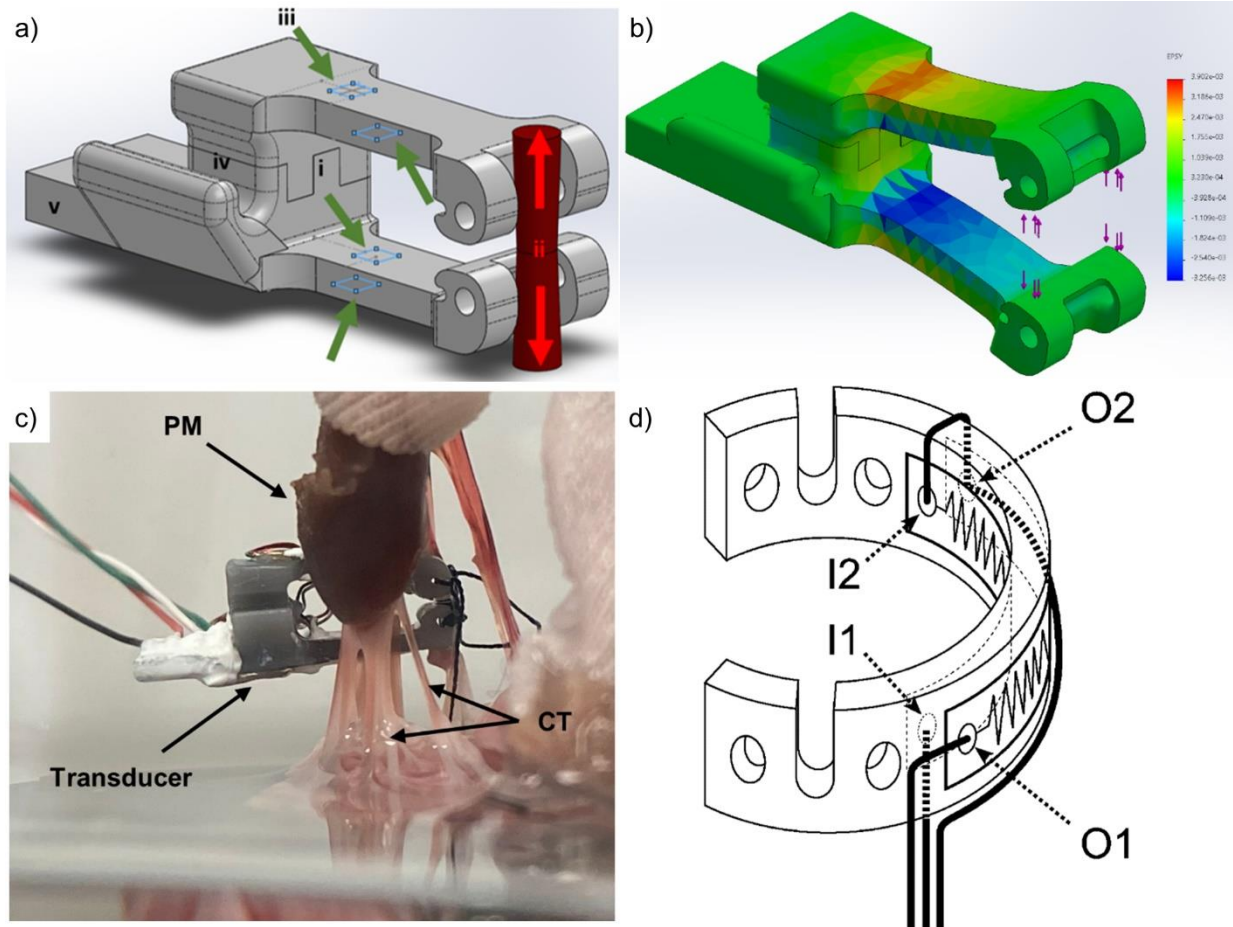


**Figure 17** – Chordal measurements transducers; a) SolidWorks model of 3D printer cantilever frame showing strain gauge placement in blue squares, b) deformation of cantilever frame under expected chordal loading, early prototype of cantilever transducer, installed onto a MV (on the vacuum system) and d) brass c-gauges [38]

The frames attach to the chordae by silk suture that is passed through several eyelets. The suture is first tied securely to the chord at the intended location. A drop of adhesive may be used to prevent slipping, though sufficient results have been obtained using fine (4-0 or 5-0) silk suture alone. The knotted suture's free ends are then passed through the frame eyelets and again

knotted, securing the frame to the chord. Once securely tied to each frame half, the chord is then cut in between the frame arms so that all chordal load is transferred to the frame.

Initial prototypes were fitted with strain gauges by Stress-Tek, the American branch of UK company Vishay Micromasurements, with whom Dr. Morten Jensen has had excellent results. Unfortunately, the results were less than satisfactory, leading to all further gauge work being done by Vishay. Through consultations with their engineers, it was decided to use N5K-06-S5024L-50C/DG/E3 strain gauges (Vishay Precision Group, Malvern, PA) in a full Wheatstone-bridge configuration. Internal connections were to be made with 42 AWG wire, bonded to the frames. These gauges have a resistance of 5000 ohms; this relatively high resistance means they require less current, therefore less power dissipation as heat occurs which dramatically lowers the heating of the frames. The mounted frames from Stress-Tek are shown in Figure 17c. At the time of writing, acquisition of the newer Vishay mounted gauges was still pending.

Despite their relatively poor quality, initial chordal force trials were nevertheless conducted using the gauges from Stress-Tek; the results of this are presented in **JCTR Stephens** [37]. After calibration via suspended laboratory weights, the gauge was sutured to a secondary chord of a mounted valve. The valve was connected to the vacuum system and closed. Strain gauge signal was acquired using a LabView 9174 cDAQ with 9237 bridge input module. The DAQ was connected to a custom-developed data logging VI in LabView via USB with a 1 kHz sample rate. An excitation voltage of 2.5 V was supplied by the 9237 module. A force of 0.285 N was measured at a corresponding pressure of 120 mmHg. While not statistically significant, this value is within clinically normal ranges.

Due to additional transducer failures, all future chordal measurements were conducted with miniate brass c-gauge transducers, which have previously been reported [38]. These gauges,

shown in Figure 17d, use the same acquisition hardware as was employed for the cantilever transducers.

### **2.5.3 Papillary Muscle Force**

Due to the limited number of working chordal transducers currently available, it was decided for the second animal trial to instead measure papillary forces. This additionally has the benefit of being a generally easier, more consistent measurement to make. While papillary forces were previously measured and reported in **JCTR, Stephens**, the system used to record the forces had room for improvement. A new apparatus was therefore built to anchor and position a pair of axial load cells. The PM force apparatus, shown in Figure 18, was constructed primarily from structural aluminum extrusion (80/20 LLC, Columbia City, IN). Translation points along several axes permit simple adjustment of the load cell positions in 3D space. A pair of miniature axial load cells (0-5lbf FSH04398, Futek, Irvine, CA) measure force. The load cells are constructed in a full-bridge configuration. Bridge excitation and data acquisition were handled through a LabView 9174 cDAQ with a 9237 bridge input module.

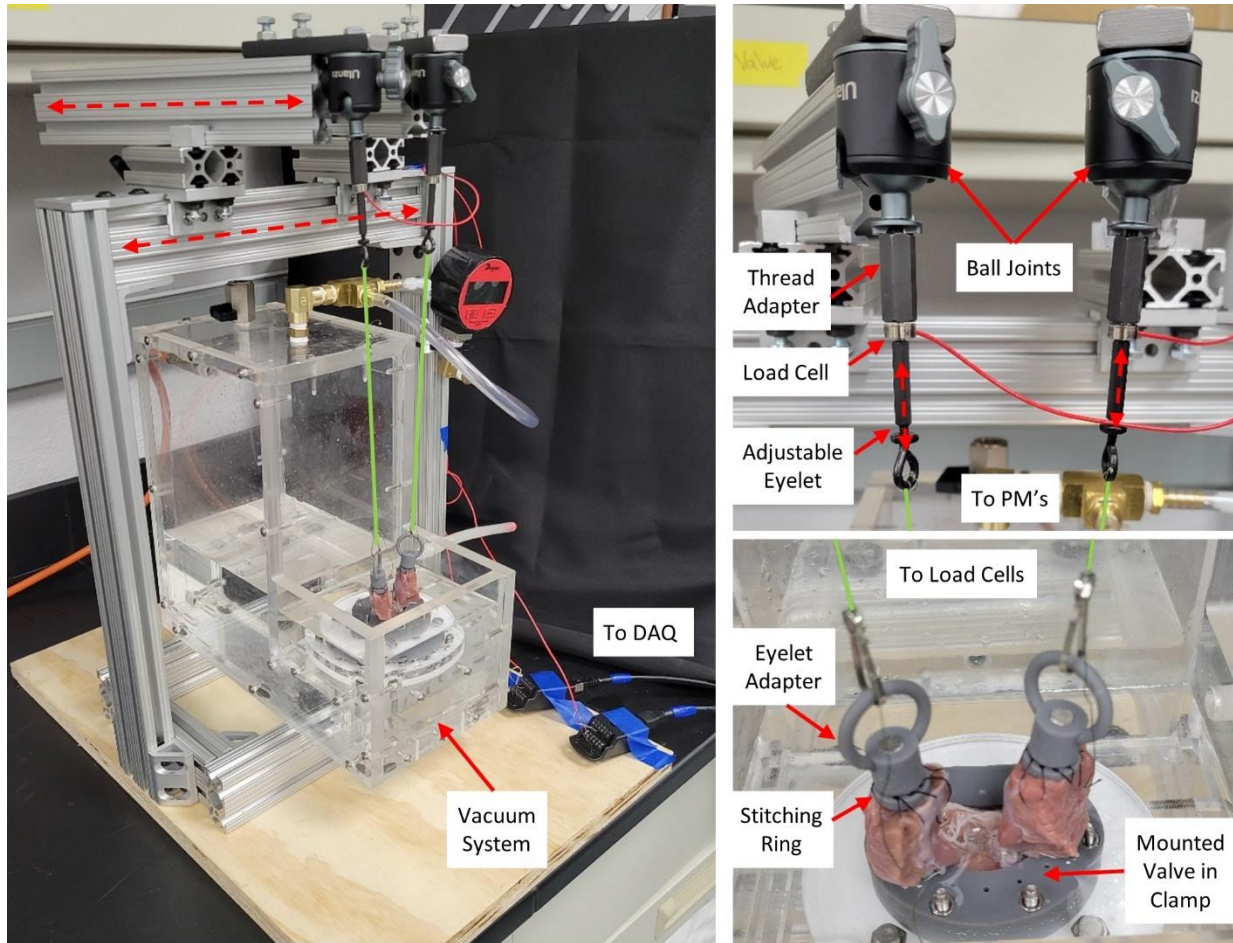


**Figure 18** – Papillary muscle force measurement apparatus; a) full apparatus with vacuum system, b) detail of load cell mounting and c) mounted valve. Tension-carrying lines are shown in green for clarity. Linear translations and adjustments are illustrated by dotted red arrows

To ensure papillary forces were exerted in-line with the load cell axes, each load cell was mounted on a lockable ball joint (U-80L, Ulanzi, Sheung Wan, Hong Kong), permitting rotation in three axes. A thread adapter was used to connect the M3 stud of the load cell to the #10-32 thread of the ball joint. The sensing stud on the other side of the load cell was connected to a coupler, into the other end of which was threaded a small eyebolt. A high-strength, inextensible line connected the eyebolts to the PM's. A small swivel was placed in each line to eliminate any twisting effects. Adjustment of the length of line from load cell to PM is made by screwing the

eyebolts further into or out of the couplers. Papillary positions were set with a jig that was custom 3D printed based on *in vivo* measurements (section 2.2). This jig temporarily connects to the annulus clamp, indexing with several reference features, and has two pins that terminate at the desired PM locations. The force apparatus is adjusted so that the tips of the mounted PM's touch the pins, placing them at their intended locations. Once set, the jig is then removed.

The vacuum system is placed within the force apparatus. The operation of the vacuum system is unchanged from the methods previously described. Adapters were made for the stitching rings to eliminate the need to swap out the ones designed for the PM holder (section 2.2) for ones with eyelets (section 2.5.1).

## **2.6 Finite Element Simulations**

A thorough discussion of the finite element simulations, for which the above-described imagery and biomechanics serve as inputs, is outside the scope of this thesis. Nevertheless, a brief summary of simulation requirements, setup and initial results are presented here to provide additional context to the above experimental methods.

For much of the project's funding period it was planned that the computational work would be handled mostly/entirely by collaborators at the University of Kentucky. Somewhat late in the project however, it became apparent that due to a variety of logistical issues, this may not be possible. For the purposes of including some initial simulation results within this document as well as for inclusion in a funding extension application, it was decided to perform finite element simulations in-house. Due to its popularity/accessibility, as well as some nice results from

collaborators using it on another project, COMSOL (COMSOL Inc., Stockholm, Sweden) was chosen to run the simulations.

### ***2.6.1 Geometry Simplification***

Given the large size of the reconstructed  $\mu$ CT datasets (upwards of 6 million vertices) and relatively limited computational power, a simplified valve geometry was created. The dataset to be simplified was first reconstructed and imported into Solidworks as a graphics body (File>Open, change filetype to mesh, Options>Graphics Body). To reduce rendering time, the display style was changed to shaded without edges. Within a 3D sketch, important anatomical landmarks were visually identified and marked by placing coordinate points directly on the model's surface. Important features include the leaflet free edges, annulus, and CT insertion points (into both the leaflets and the PMs). The multiple points along the leaflets and annulus were then connected using splines to form two separate loops. Guide curves, which follow the leaflet profile radially, were similarly created by manually placing 6-10 points along the leaflet surface, with the first and final point lying on the free edge and annular splines. Each set of guide-curve points was then connected with a separate spline. Some user discretion is necessary when determining the spacing and distribution of guide curves and reference points. Generally, a higher point/curve density is needed in regions of higher curvature. A surface, representing the simplified valve, was created using a surface loft feature where the annular and free edge spline loops define the loft profiles, and the radial-leaflet splines were used as guide curves for the loft. This process was performed on the atrial surface of the leaflets only to avoid the uneven geometry around the chordal insertion sites. The CT were not modeled directly in this simplification process.



### **2.6.2 COMSOL Modeling**

This mesh of this STL file had to be refined and geometrically scaled in Autodesk Meshmixer (Autodesk, San Rafael, CA). The mesh refinement was necessary for complex geometries, such as areas of relatively high curvature on the leaflets. The refined STL was then imported into COMSOL Multiphysics (COMSOL, Burlington, MA) and the simplified geometry constructed as a surface with shell elements representing leaflets. The leaflets were simulated as a linear elastic material with Young's modulus of 40 MPa, a Poisson's ratio of 0.495, and a density of 1100 kg/m<sup>3</sup>. Additionally, the leaflets were given a virtual thickness of 0.7 mm.

The chords were constructed as spring elements. This was done by first tracing the chords on the uCT data in SolidWorks using splines. The coordinates from the start and end points of the splines were directly implemented into the FEA model. The full length of the chords was used as the point where the stiffness/spring constant of the chords would change from approximately zero (for a chordal length less than the traced length) to a spring constant of 2200 N/m for a taut chord. A uniform pressure of 100 mmHg, approximately equal to a mid-systolic ventricular pressure, was applied on the ventricular side of the leaflets. The annulus was fixed against translation but made free to rotation while the chords were fixed at their PM ends.

### **III. Pilot Data**

Two animal trials were conducted at the University of Arkansas for Medical Sciences (UAMS) research center to test the full, above-outlined, procedure. While many aspects of the workflow had been thoroughly tested, these were the first opportunity to evaluate the *in vivo* ultrasound imaging.

To “hedge our bets”, and as the first trial somewhat corresponded to the timing of submission of a no-cost-extension for the NIH funding, several compromises were made. First, it was elected to perform ultrasound imaging epicardial, rather than through a esophageal approach. This was viewed as an easier option, particularly since nobody involved (including surgical collaborators) had used the equipment before. Additionally, for ease of placement, only one pressure catheter was used. This catheter was placed within the LV through an apical purse-string access. It was feared that placement of an atrial pressure catheter might lead to inadvertent damage to or interference with either the mitral or aortic valve, particularly since fluoroscope guidance wasn’t available. Transmitral pressure was calculated using an assumed atrial pressure of 10 mmHg [39,40].

Upon examination of the ultrasound data from the first trial, it became apparent that the entire valve has not been imaged. Retrospectively, this was apparent during imaging as the coaptation of the leaflets was visible from a long-axis perspective. To capture the entirety of the valve, a ring of ventricular wall surrounding the valve must also be imaged, obscuring such a coaptation view. This oversight was not noticed until after the pig had been euthanized and the valve dissected, so it was no longer possible to redo the ultrasound. Frustratingly, the PMs were additionally not visible within the datasets. Periodically, one or both muscles would come into view in several of the ultrasound captures, but this proved to not be helpful as there was no way to accurately register this with other captures so that the PM tips could be located in 3D space. For the second trial, a TEE approach was used for imaging. This approach was more familiar to the assisting cardiologist as this is how the majority of clinical imagery is acquired.

Once the hardware customization was completed (section 2.2.2), the custom-designed annular clamp was 3D printed. Despite the incomplete valve imagery of the first trial, the clamp still

appeared to fit the valve well. Small alumina fiducial markers (section 2.3.3) were adhered to the ventricular sides of both leaflets by first dredging the marker CA glue and then pressing against the leaflet with tweezers. Prior to mounting within the clamp, the valve was stained in Lugol's solution for 80 minutes at a 2.85% concentration (section 2.3.2). The mounted valves were loaded within the  $\mu$ CT scanning apparatus (section 2.3.1) and scanned in the open configuration. Closed-valve scanning was attempted immediately after this but was unsuccessful for the first valve due to technical issues with the pressurization system (section 2.3.4).

During the correction of the pressurization system, it was announced that the  $\mu$ CT scanner would be offline for repairs. These repairs unfortunately proved difficult to diagnose/complete, as the scanner was offline for 2 months, during which the first valve degraded past the point of being usable. While we have had success with olive oil storage, this was significantly longer than we had ever experimented with before. Therefore, a direct open-to-closed geometry comparison, for the purpose of FEA iteration, was not possible with this first study.

Due to the short time between the second animal trial and the defense of this work, a thorough FEA treatment of the second valve was not possible. Despite the relatively rough open-valve scan of the first trial (Figure 19e), a simplified geometry was successfully constructed and used to simulate closure. Many challenges still remain before simulated closure can be considered robust and reliable, yet the leaflets are tending towards closure, as illustrated in Figure 19h, which shows the "closed" leaflets from a superior/atrial view.

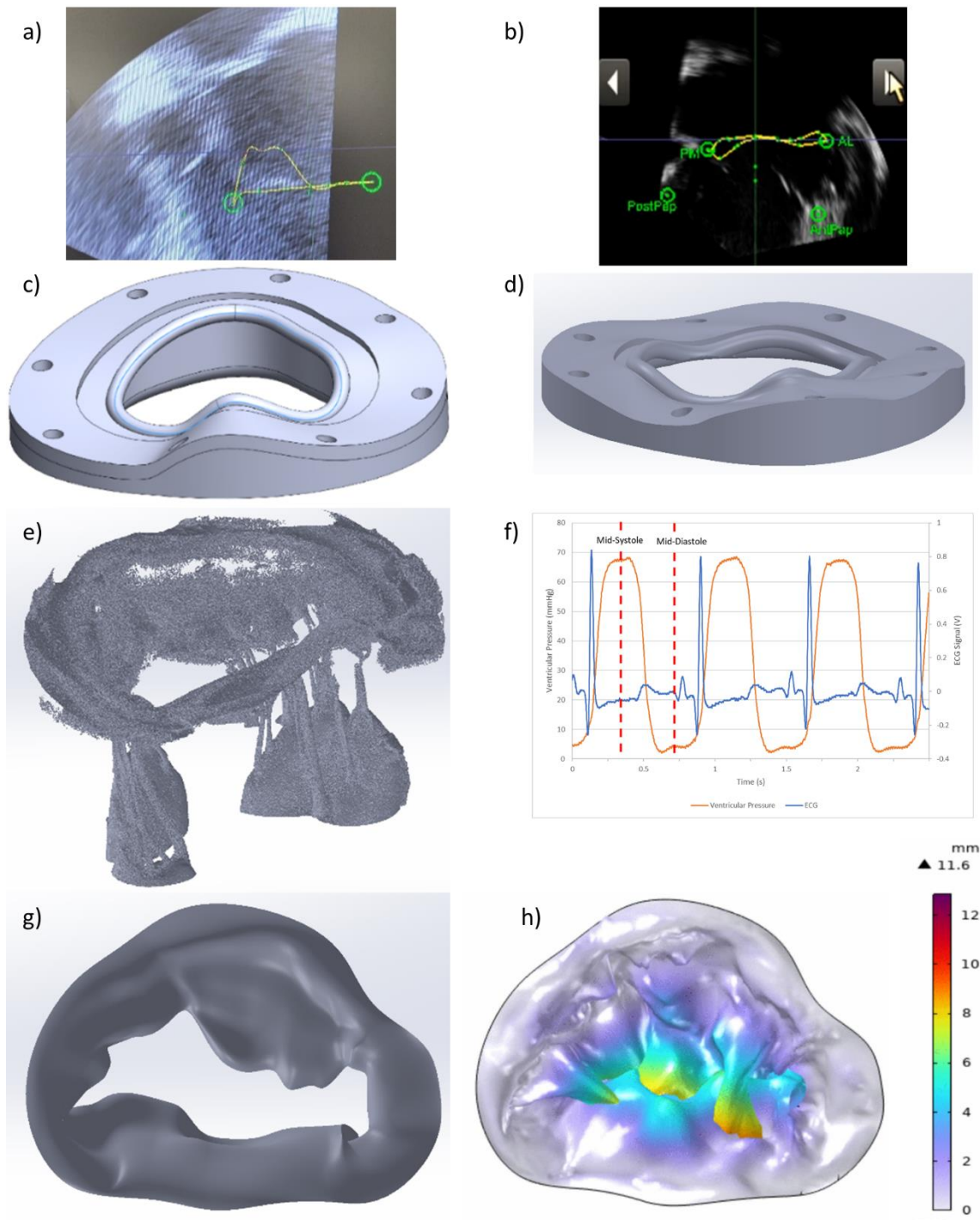


**Figure 19** – Animal trial valves; Left column is trial #1, right column is trial #2, a&b) ultrasound b-mode, c&d) customized annulus clamp, e)  $\mu$ CT 3D model, f) ECG (blue) and ventricular pressure (orange), g) simplified geometry (trial #1 only) and h) COMSOL simulations results with displacement heatmap (trial #1 only)

#### **IV. Conclusion**

The mitral valve is a complex structure that, due to its vital role within the confines of the beating heart, eludes simple, direct study. This thesis outlines a workflow that was developed to combine *in vivo* and benchtop experiments to obtain an as-complete-as-possible understanding of mitral mechanics at peak force. Three-dimensional ultrasound of the valve is obtained within the beating heart, the geometry of which is used to design and produce tailored mounting hardware on a per-valve basis. The valve, once explanted, is mounted within this hardware and high-resolution imagery obtained by  $\mu$ CT for both open and closed configurations. Subsequently, the valve is transferred to a biomechanics apparatus where fluid pressure closes the valve and chordal and/or papillary force is measured. Finally, the valvular geometry, fluid pressures and chordal forces are used as inputs for finite element simulations to iteratively determine valve tissue properties.

#### **V. Future Work**

One of the most interesting and yet also challenging aspects of this work has been that it encompasses many different disciplines, including clinical considerations, 3D imaging and image analysis, 3D printing, machining and data acquisition. While the above outlines workflow is demonstrated to be effective, there remain some challenges to overcome.

Perhaps the most apparent (potential) limitation of this work is that much of it is conducted upon explanted valves, rather than *in vivo*. It is difficult to determine whether valvular behavior is identical between *in vivo* and *in vitro*, largely due to the very challenging nature of *in vivo* measurements where virtually everything is limited – access, space, imaging resolution, etc. Any potential active response of the native valve would clearly be lost in benchtop studies, and there

is additionally the usual issue of tissue preconditioning. Perhaps future developments will render *in vivo*, high-resolution imaging possible/practical, but until then the mixture of *in vivo* and *in vitro* work, typical of other studies, will remain necessary.

Beyond this, several elements of the outlined workflow require further study. The staining process outlined in the imaging section is known to cause noticeable tissue stiffening for aggressive staining procedures. What isn't known, is how much stiffness is gained through the modest protocols followed here. Given that biomechanical measurements are to be conducted after staining, this effect should be investigated. Some initial biaxial stress-strain work has been completed (with inconclusive results) and will be continued by an undergraduate researcher. It has additionally been observed (and utilized) that valve storage in olive oil significantly delays tissue spoilage. While food preservation in olive oil is anecdotally known since ancient times, there appears to be a surprising paucity of this within scientific literature. Additional biaxial work is necessary to determine the degree of tissue changes typical to olive oil storage for moderate times; upwards of two weeks. This work is particularly relevant given the shrinkage experienced by the first study valve during oil storage.

Computational results are generally only reliable if they have been validated against physical testing. It is necessary that future modeling done in COMSOL be validated if the obtained valvular properties are to be trusted. One way in which this may be done is to utilize an artificial valve of some known material (and material properties) to perform the above workflow. The geometry and mechanics of this artificial valve can be entered into the model and the FEA results compared against the known properties.

The future should/will also include additional repetitions of the above workflow beyond the pilot data presented. Given that each valve is imaged *in vivo*, harvested, mounted, scanned both open and closed, then remounted for chordal force measurement, this represents a substantial logistical burden for each trail. Failure at any point in the workflow may jeopardize the remainder of the dataset, as evidenced in the pilot study. Many of the individual operations certainly could benefit from refinement, but the overall process is shown to be sound.

## References

1. Jesper B. Askov P, Jesper L. Hønge M, PhD, Morten O. Jensen P, Hans Nygaard D, J. Michael Hasenkam M, Sten L. Nielsen M, PhD (2013) Significance of force transfer in mitral valve–left ventricular interaction: In vivo assessment. *The Journal of Thoracic and Cardiovascular Surgery* 145 (6)
2. Omran AS, Arifi AA, Mohamed AA (2010) Echocardiography of the mitral valve. *Journal of the Saudi Heart Association* 22 (3):165-170. doi:<https://doi.org/10.1016/j.jsha.2010.04.001>
3. MayoClinic Mitral Valve Regurgitation. <https://www.mayoclinic.org/diseases-conditions/mitral-valve-regurgitation/symptoms-causes/syc-20350178>. Accessed April 22 2023
4. Stephens S, Maisonneuve MR, Liachenko S, Wenk JF, Jensen MO (2017) In Vitro Left Heart System with 7T MRI Provides High Resolution Mitral Valve 3D Imaging Datasets for Computational Modeling. *Proceedings of the 2017 Summer Biomechanics, Bioengineering and Biotransport Conference (SB3C)*:69-70
5. Gaasch WH, John RM, Aurigemma GP (1995) Managing Asymptomatic Patients With Chronic Mitral Regurgitation. *Chest* 108 (3):842-847. doi:<https://doi.org/10.1378/chest.108.3.842>
6. Nkomo VT, Gardin JM, Skelton TN, Gottdiener JS, Scott CG, Enriquez-Sarano M (2006) Burden of valvular heart diseases: a population-based study. *The Lancet* 368 (9540):1005-1011. doi:[https://doi.org/10.1016/S0140-6736\(06\)69208-8](https://doi.org/10.1016/S0140-6736(06)69208-8)
7. Nascimento R, Freitas A, Teixeira F, Pereira D, Cardoso A, Dinis M, Mendonça I (1997) Is mitral valve prolapse a congenital or acquired disease? *Am J Cardiol* 79 (2):226-227. doi:[10.1016/s0002-9149\(96\)00722-9](https://doi.org/10.1016/s0002-9149(96)00722-9)

8. Freed LA, Levy D, Levine RA, Larson MG, Evans JC, Fuller DL, Lehman B, Benjamin EJ (1999) Prevalence and Clinical Outcome of Mitral-Valve Prolapse. *New England Journal of Medicine* 341 (1):1-7. doi:10.1056/NEJM199907013410101
9. Andersen HR, Knudsen LI Fau - Hasenkam JM, Hasenkam JM Transluminal implantation of artificial heart valves. Description of a new expandable aortic valve and initial results with implantation by catheter technique in closed chest pigs. (0195-668X (Print))
10. Cribier A, Eltchaninoff H Fau - Bash A, Bash A Fau - Borenstein N, Borenstein N Fau - Tron C, Tron C Fau - Bauer F, Bauer F Fau - Derumeaux G, Derumeaux G Fau - Anselme F, Anselme F Fau - Laborde F, Laborde F Fau - Leon MB, Leon MB Percutaneous transcatheter implantation of an aortic valve prosthesis for calcific aortic stenosis: first human case description. (1524-4539 (Electronic))
11. Umukoro PE, Yeung-Lai-Wah P, Pathak S, Elkhidir S, Soodi D, Delgoffe B, Berg R, Anderson KP, Garcia-Montilla RJ (2021) Three-Year Survival after Transcatheter Aortic Valve Replacement: Findings from the Marshfield Aortic Valve Experience (MAVE) Study. *Clin Med Res* 19 (1):10-18. doi:10.3121/cmr.2020.1539
12. Potter BJ, Ann Thompson C (2019) Cost of operating room time for endovascular transcatheter aortic valve replacement. *Journal of Medical Economics* 22 (10):1022-1024. doi:10.1080/13696998.2019.1627364
13. Rotman OM, Bianchi M, Ghosh RP, Kovarovic B, Bluestein D (2018) Principles of TAVR valve design, modelling, and testing. *Expert Rev Med Devices* 15 (11):771-791. doi:10.1080/17434440.2018.1536427
14. Testa L, Popolo Rubbio A, Casenghi M, Pero G, Latib A, Bedogni F (2019) Transcatheter Mitral Valve Replacement in the Transcatheter Aortic Valve Replacement Era. *Journal of the American Heart Association* 8 (22):e013352. doi:10.1161/JAHA.119.013352
15. Gammie JS, Sheng S Fau - Griffith BP, Griffith Bp Fau - Peterson ED, Peterson Ed Fau - Rankin JS, Rankin Js Fau - O'Brien SM, O'Brien Sm Fau - Brown JM, Brown JM Trends in mitral valve surgery in the United States: results from the Society of Thoracic Surgeons Adult Cardiac Surgery Database. (1552-6259 (Electronic))
16. Ramlawi B, Skiles J, Myers D, Ali O, Viens C (2018) Transcatheter mitral repair: MitraClip technique. *Annals of cardiothoracic surgery* 7 (6):824-826. doi:10.21037/acs.2018.10.14



17. Sotolongo A, Bin Mahmood SU, Vaccaro B, Geirsson A (2020) Mitral valve repair using adjustable posterior leaflet neochords. *JTCVS Techniques* 2:50-54. doi:10.1016/j.xjtc.2020.02.013
18. Toma M, Jensen MO, Einstein DR, Yoganathan AP, Cochran RP, Kunzelman KS (2016) Fluid-Structure Interaction Analysis of Papillary Muscle Forces Using a Comprehensive Mitral Valve Model with 3D Chordal Structure. *Ann Biomed Eng* 44 (4):942-953. doi:10.1007/s10439-015-1385-5
19. Votta E, Caiani E Fau - Veronesi F, Veronesi F Fau - Soncini M, Soncini M Fau - Montevecchi FM, Montevecchi Fm Fau - Redaelli A, Redaelli A Mitral valve finite-element modelling from ultrasound data: a pilot study for a new approach to understand mitral function and clinical scenarios. (1364-503X (Print))
20. Einstein DR, Kunzelman Ks Fau - Reinhall PG, Reinhall Pg Fau - Nicosia MA, Nicosia Ma Fau - Cochran RP, Cochran RP Non-linear fluid-coupled computational model of the mitral valve. (0966-8519 (Print))
21. McCarthy KP, Ring L, Rana BS (2010) Anatomy of the mitral valve: understanding the mitral valve complex in mitral regurgitation. *European Journal of Echocardiography* 11 (10):i3-i9. doi:10.1093/ejechocard/jeq153
22. May-Newman K, Yin FC (1995) Biaxial mechanical behavior of excised porcine mitral valve leaflets. *American Journal of Physiology-Heart and Circulatory Physiology* 269 (4):H1319-H1327. doi:10.1152/ajpheart.1995.269.4.H1319
23. Cochran RP, Kunzelman Ks Fau - Chuong CJ, Chuong Cj Fau - Sacks MS, Sacks Ms Fau - Eberhart RC, Eberhart RC Nondestructive analysis of mitral valve collagen fiber orientation. (0889-7190 (Print))
24. Zuo K, Pham T, Li K, Martin C, He Z, Sun W (2016) Characterization of biomechanical properties of aged human and ovine mitral valve chordae tendineae. *J Mech Behav Biomed Mater* 62:607-618. doi:10.1016/j.jmbbm.2016.05.034
25. Jimenez J, Liou S, Padala M, He Z, Sacks M, Gorman R, GormanIII J, Yoganathan A (2007) A saddle-shaped annulus reduces systolic strain on the central region of the mitral valve anterior leaflet. *The Journal of Thoracic and Cardiovascular Surgery* 134 (6):1562-1568

26. Jimenez JH, Soerensen Dd Fau - He Z, He Z Fau - Ritchie J, Ritchie J Fau - Yoganathan AP, Yoganathan AP Effects of papillary muscle position on chordal force distribution: an in-vitro study. (0966-8519 (Print))
27. Easley TF, Bloodworth CHt, Bhal V, Yoganathan AP (2018) Effects of annular contraction on anterior leaflet strain using an in vitro simulator with a dynamically contracting mitral annulus. *Journal of biomechanics* 66:51-56. doi:10.1016/j.jbiomech.2017.10.045
28. Bloodworth CHt, Pierce EL, Easley TF, Drach A, Khalighi AH, Toma M, Jensen MO, Sacks MS, Yoganathan AP (2017) Ex Vivo Methods for Informing Computational Models of the Mitral Valve. *Ann Biomed Eng* 45 (2):496-507. doi:10.1007/s10439-016-1734-z
29. Ostli B, Vester-Petersen J, Askov J, Hønge J, Levine R, Hagège A, Nielsen S, Hasenkam J, Nygaard H, Jensen M (2012) In Vitro System for Measuring Chordal Force Changes Following Mitral Valve Patch Repair. *Cardiovascular Engineering and Technology* 3 (3):263-268. doi:10.1007/s13239-012-0098-2
30. Hosny A, Shen T, Kuo AS, Long D, Andrawes MN, Dilley JD (2018) Unlocking vendor-specific tags: Three-dimensional printing of echocardiographic data sets. *J Thorac Cardiovasc Surg* 155 (1):143-145 e141. doi:10.1016/j.jtcvs.2017.08.064
31. Stephens SE, Liachenko S, Ingels NB, Wenk JF, Jensen MO (2017) High resolution imaging of the mitral valve in the natural state with 7 Tesla MRI. *Plos One* 12 (8)
32. Pierce EL, Bloodworth CHt, Naran A, Easley TF, Jensen MO, Yoganathan AP (2016) Novel Method to Track Soft Tissue Deformation by Micro-Computed Tomography: Application to the Mitral Valve. *Ann Biomed Eng* 44 (7):2273-2281. doi:10.1007/s10439-015-1499-9
33. Stephens SE, Bean M, Surber H, Ingels NB, Jensen HK, Liachenko S, Wenk JF, Jensen MO (2021) MicroCT Imaging of Heart Valve Tissue in Fluid. *Exp Mech* 61 (1):253-261. doi:10.1007/s11340-020-00667-5
34. Rabbah J-P, Saikrishnan N, Yoganathan AP (2013) A Novel Left Heart Simulator for the Multi-modality Characterization of Native Mitral Valve Geometry and Fluid Mechanics. *Annals of Biomedical Engineering* 41 (2):305-315. doi:10.1007/s10439-012-0651-z
35. Ingels NB, Daughters GT, Stinson EB, Alderman EL (1975) Measurement of midwall myocardial dynamics in intact man by radiography of surgically implanted markers. *Circulation* 52 (5):859-867. doi:10.1161/01.CIR.52.5.859

36. Stephens SE, Ingels NB, Wenk JF, Jensen MO (2022) Alumina as a Computed Tomography Soft Material and Tissue Fiducial Marker. *Experimental Mechanics*. doi:10.1007/s11340-022-00825-x

37. Stephens SA-O, Kammien AA-O, Paris JA-O, Applequist AP, Ingels NB, Jensen HA-O, Rodgers DE, Cole CR, Wenk JA-O, Jensen MA-O In Vitro Mitral Valve Model with Unrestricted Ventricular Access: Using Vacuum to Close the Valve and Enable Static Trans-Mitral Pressure. LID - 10.1007/s12265-021-10199-5 [doi]. (1937-5395 (Electronic))

38. Nielsen SL, Soerensen DD, Libergren P, Yoganathan AP, Nygaard H (2004) Miniature C-Shaped Transducers for Chordae Tendineae Force Measurements. *Annals of Biomedical Engineering* 32 (8):1050-1057. doi:10.1114/B:ABME.0000036641.69903.62

39. Kircher BJ, Himelman RB, Schiller NB (1990) Noninvasive estimation of right atrial pressure from the inspiratory collapse of the inferior vena cava. *Am J Cardiol* 66 (4):493-496. doi:10.1016/0002-9149(90)90711-9

40. Li B, Cui Y, Zhang D, Luo X, Luo F, Li B, Tang Y (2018) The characteristics of a porcine mitral regurgitation model. *Experimental Animals* 67 (4):463-477. doi:10.1538/expanim.18-0045

## Appendix A – List of Relevant Publications (Chronological)

- **Stephens SE**, Liachenko S, Ingels NB, Wenk JF, Jensen MO (2017) High resolution imaging of the mitral valve in the natural state with 7 Tesla MRI. PLoS ONE 12(8): e0184042. <https://doi.org/10.1371/journal.pone.0184042>
- **Stephens, S.**, Bean, M., Surber, H. et al. MicroCT Imaging of Heart Valve Tissue in Fluid. *Experimental Mechanics* (2020). <https://doi.org/10.1007/s11340-020-00667-5>
- **Stephens SE\***, Kammien AJ\*, Ingels NB, Jensen HK, Jensen MO, In Vitro Mitral Valve Model with Unrestricted Ventricular Access: Using Vacuum to Close the Valve and Enable Static Trans-Mitral Pressure. *Journal of Cardiovascular Translational Research* (2022). doi: 10.1007/s12265-021-10199-5
- **Stephens SE**, Ingels NB, Wenk JF, Jensen MO, Alumina as a Computer Tomography Soft Material and Tissue Fiducial Marker. <https://doi.org/10.1007/s11340-022-00825-x>
- **Stephens SE**, Henry K, Wenk JF, Jensen MO, Semi-Automatic Removal of Mounting Hardware from Mitral Valve 3D Datasets. In Progress
- **Stephens SE**, Ingels NB, Wenk JF, Jensen MO, STL-Stitching. In Progress

## Appendix B – Fiducial Localization Mathematics

### *Mathematical Derivation and Details*

Consider a collection of fiducial points that rotate about the vertical axis on a turntable. Let the origin of the manipulator coordinate frame, denoted  $M$ , lie at the center of the turntable with  $M_1$  oriented towards the detector,  $M_2$  parallel to the detector and  $M_3$  vertically upwards. The orientations of  $M_1$  and  $M_2$  do not change as the turntable rotates. The spatial relationships of the scanner point source, turntable and detector plane are shown in Figure A1. Add in discussion of image and case coordinate systems.

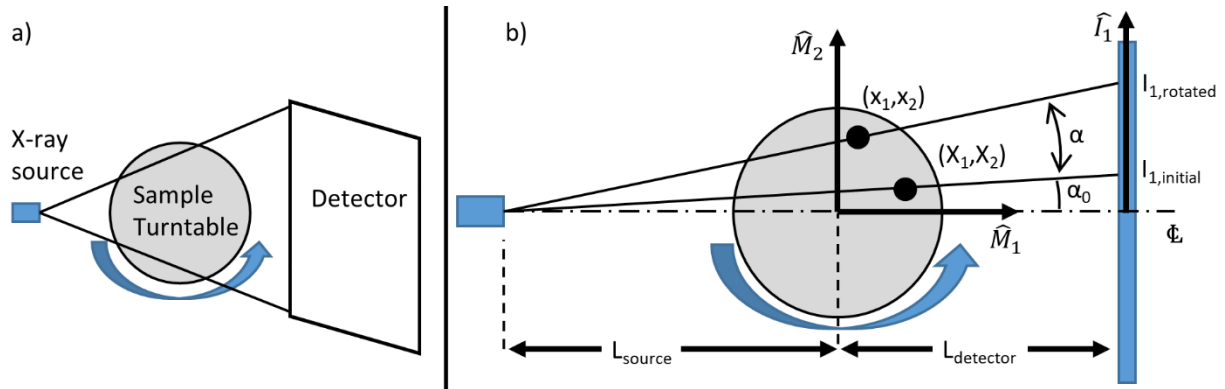


**Figure A1** – a) Schematic view of imaging setup and b) definitions of coordinate axes

For a given fiducial marker, the initial manipulator-frame coordinates are  $(X_1, X_2, X_3)$ . These can be expressed in cylindrical coordinates as:

$$X_1 = R \cos(\alpha_0)$$

(1)

$$X_2 = R \sin(\alpha_0)$$

(2)

Where  $R$  is the radial distance from the center of rotation and  $\alpha_0$  is the azimuthal angle from the  $M_1$  axis. The same point, after a rotation  $\alpha$ , will have rotated coordinates  $(x_1, x_2, x_3)$  where:

$$x_1 = R \cos(\alpha_0 + \alpha) \quad (3)$$

$$x_2 = R \sin(\alpha_0 + \alpha) \quad (4)$$

$$x_3 = X_3 \quad (5)$$

Using the trigonometric identities (6) and (7) for angle addition, the rotated coordinates can be expressed in terms of the initial un-rotated coordinates and  $\alpha$ .

$$\sin(A + B) = \sin(A) \cos(B) + \cos(A) \sin(B)$$

(6)

$$\cos(A + B) = \cos(A) \cos(B) - \sin(A) \sin(B)$$

(7)

$$x_1 = R \cos(\alpha_0) \cos(\alpha) - R \sin(\alpha_0) \sin(\alpha) \quad (8)$$

$$\boxed{x_1 = X_1 \cos(\alpha) - X_2 \sin(\alpha)} \quad (9)$$

$$x_2 = R \sin(\alpha_0) \cos(\alpha) + R \cos(\alpha_0) \sin(\alpha) \quad (10)$$

$$\boxed{x_2 = X_2 \cos(\alpha) + X_1 \sin(\alpha)} \quad (11)$$

Thus the rotated coordinates are determined only by the initial locations and the rotated angle.

By examining images taken before and after rotation, the rotated coordinates, and therefore the initial coordinates, may be determined. Consider the scanner setup prior to and after rotation, illustrated from the top view, in Figure A2.

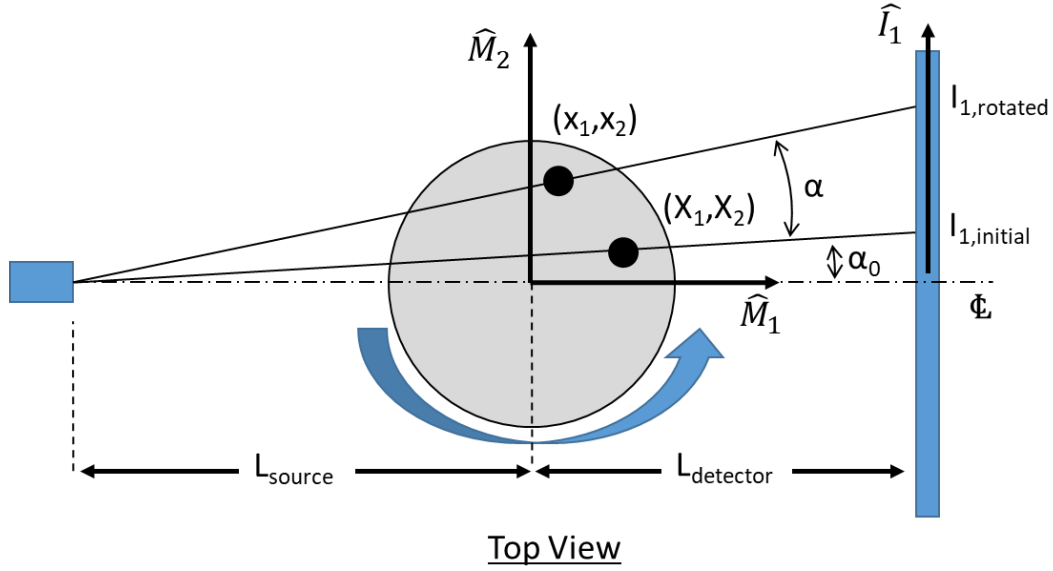


**Figure A2** – Top view of a) pre and post rotation imaging configurations - add in b) detail of triangle #1, c) detail of triangle #2

The tangent of the angle formed between the centerline and the ray passing through the initial point location (detail shown in Figure A2b) can be expressed as:

$$\tan(\alpha_0) = \frac{I_{1,initial}}{L_{source} + L_{detector}} \quad (12)$$

Where  $I_{1,initial}$  is the location within the image coordinate system, denoted  $\mathbf{I}$ , of the projection from the initial point location. Similarly, for the rotated location:

$$\tan(\alpha_0 + \alpha) = \frac{I_{1,rotated}}{L_{source} + L_{detector}}$$

(13)

Solving equations (12) and (13) for the projection in the image coordinate system:

$$I_{1,initial} = \tan(\alpha) (L_{source} + L_{detector})$$

(14)

$$I_{1,rotated} = \tan(\alpha_0 + \alpha) (L_{source} + L_{detector})$$

(15)

The movement in the  $I_1$  direction due to rotation  $\alpha$  is therefore:

$$\Delta I_1 = I_{1,rotated} - I_{1,initial} \tag{16}$$

$$\Delta I_1 = (L_{source} + L_{detector})(\tan(\alpha_0 + \alpha) - \tan(\alpha_0))$$

(17)

The rays through the initial and rotated points also define the hypotenuses of similar triangles shown in Figure A2c such that:

$$\tan(\alpha_0) = \frac{X_2}{L_{source} + X_1} \tag{18}$$

$$\tan(\alpha_0 + \alpha) = \frac{x_2}{L_{source} + x_1} \tag{19}$$

Substitution of these relations into equation (17) yields:

$$\Delta I_1 = (L_{source} + L_{detector}) \left( \frac{x_2}{L_{source} + x_1} - \frac{X_2}{L_{source} + X_1} \right) \tag{20}$$

Substitution of equations (9) and (11) allows  $\Delta I_1$  to be expressed only in terms of the initial point locations:

$$\boxed{\Delta I_1 = (L_{source} + L_{detector}) \left( \frac{X_2 \cos(\alpha) + X_1 \sin(\alpha)}{L_{source} + X_1 \cos(\alpha) - X_2 \sin(\alpha)} - \frac{X_2}{L_{source} + X_1} \right)}$$

(21)



Solving (21) analytically for  $X_1$  and  $X_2$  is nontrivial, however the equality may be easily solved numerically.

The vertical movement of the fiducial point's projection onto the detector plane may be determined by first examining the imaging setup from the front view, shown in Figure A3.

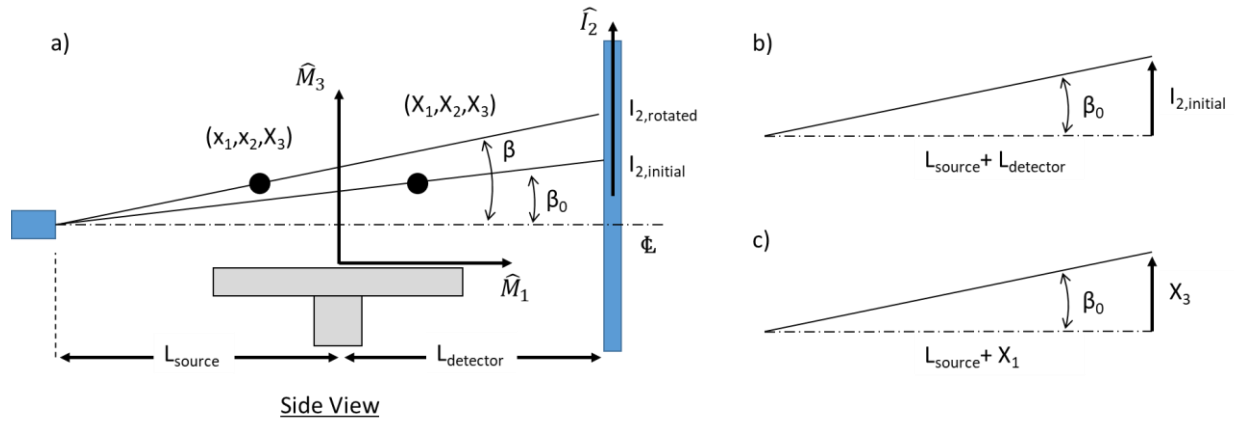


**Figure A3** – a) Front view of pre and post-rotation imaging configurations, b) Triangle #1 detail and c) Triangle #2 detail

A similar approach is employed as was used to determine the horizontal movement of the projection. Note that the point's vertical height is the same before and after rotation since rotation is about the vertical axis. The tangent of the angles formed between the centerline and the ray passing through the initial and final point locations respectively (geometric details shown in Figure A3c) can be expressed as:

$$\tan(\beta_0) = \frac{I_{2,initial}}{L_{source} + L_{detector}} \quad (22)$$

$$\tan(\beta) = \frac{I_{2,rotated}}{L_{source} + L_{detector}} \quad (23)$$

Solving equations (12) and (13) for the projection in the image coordinate system:

$$I_{2,initial} = \tan(\beta_0) (L_{source} + L_{detector}) \quad (24)$$

$$I_{2,rotated} = \tan(\beta) (L_{source} + L_{detector}) \quad (25)$$

The movement in the  $I_1$  direction due to rotation  $\alpha$  is therefore:

$$\Delta I_2 = I_{2,rotated} - I_{2,initial} \quad (26)$$

$$\Delta I_2 = (L_{source} + L_{detector})(\tan(\beta) - \tan(\beta_0))$$

$$(27)$$

The angles  $\beta_0$  and  $\beta$  similarly form a second set of triangles (shown in Figure A3c) such that:

$$\tan(\beta_0) = \frac{X_3}{L_{source} + X_1} \quad (28)$$

$$\tan(\beta) = \frac{X_3}{L_{source} + X_1} \quad (29)$$

Substitution of these relations into equation (27) yields:

$$\Delta I_2 = (L_{source} + L_{detector}) \left( \frac{X_3}{L_{source} + X_1} - \frac{X_3}{L_{source} + X_1} \right) \quad (30)$$

Substitution of (9) permits  $\Delta I_2$  to be expressed only in terms of the initial point locations:

$$\Delta I_2 = (L_{source} + L_{detector}) \left( \frac{X_3}{L_{source} + X_1 \cos(\alpha) - X_2 \sin(\alpha)} - \frac{X_3}{L_{source} + X_1} \right) \quad (31)$$

As  $X_1$  and  $X_2$  may be obtained numerically from (21), the only unknown present within (31) is

$X_3$ . Solving for  $X_3$  yields:

$$X_3 = \frac{\Delta I_2}{L_{source} + L_{detector}} \left( \frac{1}{L_{source} + X_1 \cos(\alpha) - X_2 \sin(\alpha)} - \frac{1}{L_{source} + X_1} \right)^{-1}$$

(32)

### Measurement of Projection Movement

At least two projection images are required to obtain the image-plane movement of point projections,  $\Delta I_1$  and  $\Delta I_2$ . The fiducial point's centroid is determined and the vertical and horizontal movements between images calculated as depicted in Figure A4. Determination of centroids may be manual or automatic, such as by \_\_\_\_\_ method. This procedure should be repeated for at least two pairs of images to obtain two sets of projection movements,  $(\Delta I_{1,a}; \Delta I_{2,a})$  and  $(\Delta I_{1,b}; \Delta I_{2,b})$ . The rotation from the first image to the second needn't be the same as the rotation from the second image to the third.

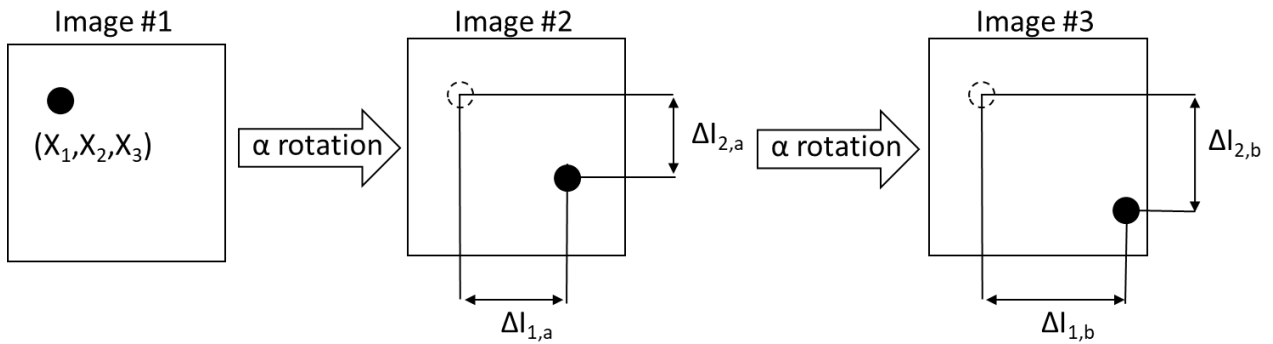


**Figure A4** – Illustrated method of measuring projection movements. The dotted circle in Image #2 and #3 denotes the initial projection location

### Numerical Methods

Equation (21) is rearranged such that the LHS equals zero:

$$F = 0 = (L_{source} + L_{detector}) \left( \frac{X_2 \cos(\alpha) + X_1 \sin(\alpha)}{L_{source} + X_1 \cos(\alpha) - X_2 \sin(\alpha)} - \frac{X_2}{L_{source} + X_1} \right) - \Delta I_1$$

(33)

An objective function F is equated to the RHS of (33). This function will be minimized numerically to find  $X_1$  and  $X_2$ .

Since (33) contains two unknowns ( $X_1$  and  $X_2$ ), a second  $\Delta I_1$  must be obtained from a second set of projection images, which must include the original projection image as a member. This establishes the following system of nonlinear equations:

$$F(1) = (L_{source} + L_{detector}) \left( \frac{X_2 \cos(\alpha_1) + X_1 \sin(\alpha_1)}{L_{source} + X_1 \cos(\alpha_1) - X_2 \sin(\alpha_1)} - \frac{X_2}{L_{source} + X_1} \right) - \Delta I_{1,a}$$

(33)

$$F(2) = (L_{source} + L_{detector}) \left( \frac{X_2 \cos(\alpha_2) + X_1 \sin(\alpha_2)}{L_{source} + X_1 \cos(\alpha_2) - X_2 \sin(\alpha_2)} - \frac{X_2}{L_{source} + X_1} \right) - \Delta I_{1,b}$$

(34)

The above system of equations may be solved by many means, including Matlab's 'fsolve' function.

function F = InitialPoints(X)

F(1) = (Ls+Ld)\*(((X(1)\*sind(a1)+X(2)\*cosd(a1))/(Ls+X(1)\*cosd(a1)-X(2)\*sind(a1)))-  
(X(2)/(Ls+X(1))))-I1a;

F(2) = (Ls+Ld)\*(((X(1)\*sind(a2)+X(2)\*cosd(a2))/(Ls+X(1)\*cosd(a2)-X(2)\*sind(a2)))-  
(X(2)/(Ls+X(1))))-I1b;

>>fun = @root2d;

```
>>X0=[0,0];
```

```
>>X=fsolve(fun,X0)
```

Where:

$L_s=L_{\text{source}}$

$L_d=L_{\text{detector}}$

$a_1=\alpha_1$

$a_2=\alpha_2$

$X_0$ =initial guess for  $[X_1, X_2, X_3]$

## Appendix C – IACUC Protocol



UNIVERSITY OF  
ARKANSAS

College of Engineering  
Department of Biomedical Engineering

### APPROVAL OF SUBMISSION

July 20, 2022

Hanna Jensen  
4301 W Markham  
Slot 520  
Pulaski  
Little Rock, AR 72205-7101

5015266990  
HKJENSEN@UAMS.EDU

Dear Hanna Jensen:

On 7/15/2022, the IACUC reviewed the following submission:

Type of Review:	New Protocol Application
Title of Protocol:	ACRI Heart Valve Force study
Investigator:	Hanna Jensen
IACUC ID:	IPROTO202200000139
Funding:	Name: NIH/National Institutes of Health, Grant Office ID: , Funding Source ID:
Documents Reviewed:	Name: animal section from Grant Name: Morten Jensen Name: Literature search uams Name: ACRI AUP form 8.14.19

The protocol is approved as of 7/15/2022. Your next annual review is due 7/14/2023.  
Your next triennial review is due 7/14/2025.

Sincerely,  
Jerry Ware  
IACUC Chair